



저작자표시-비영리-변경금지 2.0 대한민국

이용자는 아래의 조건을 따르는 경우에 한하여 자유롭게

- 이 저작물을 복제, 배포, 전송, 전시, 공연 및 방송할 수 있습니다.

다음과 같은 조건을 따라야 합니다:



저작자표시. 귀하는 원저작자를 표시하여야 합니다.



비영리. 귀하는 이 저작물을 영리 목적으로 이용할 수 없습니다.



변경금지. 귀하는 이 저작물을 개작, 변형 또는 가공할 수 없습니다.

- 귀하는, 이 저작물의 재이용이나 배포의 경우, 이 저작물에 적용된 이용허락조건을 명확하게 나타내어야 합니다.
- 저작권자로부터 별도의 허가를 받으면 이러한 조건들은 적용되지 않습니다.

저작권법에 따른 이용자의 권리는 위의 내용에 의하여 영향을 받지 않습니다.

이것은 [이용허락규약\(Legal Code\)](#)을 이해하기 쉽게 요약한 것입니다.

[Disclaimer](#)

이학석사학위논문

**Experimental Study on the Crystallographic
Preferred Orientation (CPO) of Amphibole and Its
Implications for Seismic Anisotropy**

**각섬석의 격자선호방향과
지진파 비등방성에 대한 실험연구**

2014년 8월

서울대학교 대학원

지구환경과학부

고병관

**Experimental Study on the Crystallographic Preferred
Orientation (CPO) of Amphibole and Its Implications for
Seismic Anisotropy**

각섬석의 격자선호방향과
지진파 비등방성에 대한 실험연구

지도교수 정 해 명

이 논문을 이학석사학위논문으로 제출함

2014년 8월

서울대학교 대학원

지구환경과학부

고 병 관

고병관의 이학석사 학위논문을 인준함

2014년 8월

위원장 이 준 기 (인)

부위원장 정 해 명 (인)

위원 길 영 우 (인)



Abstract

Strong seismic anisotropy in the deep crust and upper mantle is considered mainly due to the crystallographic preferred orientation (CPO) of anisotropic minerals, which can be formed by deformation. Inferring seismic properties by using CPO can provide key information on the rheology of the deep Earth. However, experimental studies on the development of CPO of anisotropic minerals in simple-shear deformation has been limited. Simple shear is considered to be the dominant mode of deformation in the crust and uppermost mantle, whereas previous studies have focused on the effects of uniaxial compression. Here, we show the results of simple-shear deformation experiments on amphibolite, conducted at the pressure of 1 GPa and temperatures of 480 to 700 °C which are amphibolite facies conditions. For large strains up to 570 %, our experiments produced three types of CPOs of amphibole, in which (100) poles align subnormal to the shear plane. Type-I CPO shows that [001] axes are aligned nearly parallel to the shear direction, which is commonly observed in highly deformed mid- to lower-crust rocks. Type-I CPO was formed at low temperatures (480 to 550 °C), and at middle temperatures (590 to 600 °C) with low differential stress (below 60 MPa). Type-II CPO represents that [010] axes are aligned nearly parallel to the shear direction. Type-II was formed at middle to high temperatures (590 to 700 °C)

with high differential stress (above 110 MPa). Type-III CPO displays that (010) poles and [001] axes form a great circle girdle subparallel to the shear plane. Type-III was observed at high temperatures (640 to 700 °C) with low differential stress (below 130 MPa). Type-II and –III CPOs are rarely found in natural samples. Seismic anisotropy was calculated from the CPO data, finding that seismic anisotropy of amphibole can be sensitive to the temperature, differential stress, and flow geometry in the deep crust and upper mantle where amphibole is stable.

Keywords: amphibolite, hornblende, crystallographic preferred orientation, seismic anisotropy, deformation experiment in simple shear, modified Griggs apparatus

Student Number: 2011-20358

Table of Contents

Abstract i

Table of Contents iii

List of Tables vi

List of Figures vii

Chapter 1. Introduction 1

Chapter 2. Previous studies

2.1 Seismic velocity and anisotropy found in the middle to lower
crust **3**

2.2 CPO of amphibole in natural rocks **5**

2.3 Experimental studies on the deformation of amphibolite **6**

Chapter 3. Starting material 10

Chapter 4. Experimental method

4.1 Measurement of sample composition. **14**

4.2 Shear deformation experiment **14**

4.3 Observation of specimen using BSE image	16
4.4 Measurement of CPO of amphibole and calculation of seismic anisotropy	16

Chapter 5. Results

5.1 Mechanical data	22
5.2 Microstructures	22
5.3 CPOs of amphibole	23
5.4 Seismic anisotropy	24

Chapter 6. Discussion

6.1 Deformation mechanism	48
6.2 The development of CPOs of hornblende	50
6.3 Water-induced weakening of amphibolite	52
6.4 Implications for seismic anisotropy	53

Chapter 7. Conclusion	64
------------------------------------	-----------

References 66

국문요약 75

List of Tables

Table 1. The composition of major minerals in the starting material.	11
Table 2. Experimental conditions and results.	18
Table 3. Results of seismic anisotropy	27

List of Figures

Figure 1. Pole figures of CPOs of naturally deformed amphibole in previous studies.	9
Figure 2. Photographs of starting material.	12
Figure 3. A photomicrograph (a), and a BSE image (b) of starting material.	13
Figure 4. A schematic figure of sample assembly.	19
Figure 5. A schematic figure of amphibolite sample inside Ni or Pt jacket.	20
Figure 6. Parts of sample assembly used in the experiment (JH72).	21
Figure 7. Strength-temperature diagram of deformed amphibolites.	28
Figure 8. BSE images of deformed amphibolite (JH54).	29
Figure 9. BSE images (a, b) of deformed amphibolite (JH72).	30
Figure 10. BSE images of deformed amphibolites (JH74, JH75).	31
Figure 11. Pole figures of crystallographic preferred orientation (CPO) of	

deformed amphibole.	32
Figure 12. Seismic anisotropy of deformed amphibole in the horizontal flow.	35
Figure 13. Seismic anisotropy of deformed amphibole for the flow dipping at 30 ° from the horizontal flow.	38
Figure 14. Seismic anisotropy of deformed amphibole for the flow dipping at 45 ° from the horizontal flow.	41
Figure 15. Seismic anisotropy of deformed in the vertical flow.	44
Figure 16. Seismic anisotropy of deformed amphibole (JH54) for four different flow geometries.	47
Figure 17. Schematic diagrams with BSE images of deformed amphibolites.	57
Figure 18. Schematic diagrams of plagioclase and hornblende at deformation stage2.	58
Figure 19. BSE images of the deformed amphibolite.	59
Figure 20. A fabric diagram for deformed amphibole.	60

Figure 21. Pole figures of typical CPO types of deformed amphibole. **61**

Figure 22. Schematic diagram of crystallographic axes and velocities. **62**

Figure 23. Schematic diagrams showing the polarization direction of shear wave for different flow geometries. **63**

Chapter 1. Introduction

Investigating factors constraining seismic anisotropy in the crust is truly important because seismic anisotropy can be a useful tool to image the structure of the crust and to understand deformation style (e.g. Ozacar and Zandt, 2004). Several factors causing the crustal seismic anisotropy have been suggested by previous studies. In the upper crust, seismic anisotropy is attributed to micro-fracturing, but that in the middle to lower crust is attributed to crystallographic preferred orientation (CPO or fabric) of anisotropic minerals because of higher pressure in such depth at which fractures are closed (e.g. Rasolofosaon et al., 2000). Some studies argued that the CPO of mica can account for seismic anisotropy in the deep crust (Shapiro et al., 2004; Mahan, 2006; Meissner et al., 2006; Lloyd et al., 2009), based on its high anisotropies: anisotropy of P-wave velocity (AV_p) up to 57 % and anisotropy of S-wave velocity (AV_s) up to 72 % (for biotite; Barruol and Mainprice, 1993). However, considering global scale of the crust, amphibole is more appropriate to explain the seismic anisotropy (Siegesmund et al., 1989; Mainprice and Nicolas, 1989; Weiss et al., 1999; Tatham et al., 2008; Moschetti et al., 2010) despite its smaller anisotropy up to $AV_p = 27.1$ % and $AV_s = 30.7$ % (Aleksandrov and Ryzhova, 1961) than that of mica—but, still much higher than anisotropies of other major minerals in the crust. This is because

amphibole is the most abundant mineral in the deep crust at amphibolite facies (~60 %), whereas the rest is mostly comprised by quartz and feldspar whose CPO strength is generally too weak to produce the strong seismic anisotropy (Tatham et al., 2008).

The previous studies of the CPO of deformed amphibole, however, have not been consistent with one another in terms of the formation condition of each CPO type of amphibole. Furthermore, the relationship between different types of the CPO of amphibole and resultant seismic anisotropy has been limited by the lack of experimental studies on the development of CPOs under deformation, especially in simple shear which is the dominant mode of deformation in nature.

Therefore, we carried out a series of deformation experiments of amphibolite in simple shear by using a modified Griggs apparatus at the pressure of 1 GPa and temperatures of 480 to 700 °C which correspond to conditions of the lower crust and uppermost mantle in amphibolite facies. Our results show that the development of three different CPO types of amphibole depend on temperature and stress during deformation, and that seismic anisotropies corresponding to the obtained CPO types depend on flow geometry.

Chapter 2. Previous studies

2.1 Seismic velocity and anisotropy found in the middle to lower crust

Previous studies of seismic velocity showed that in the middle crust, P-wave velocity and S-wave velocity on average were $V_p = 6.6 \pm 0.1$ km/s and $V_s = 3.8 \pm 0.1$ km/s, respectively, and in the lower crust, P-wave velocity and S-wave velocity on average were $V_p = 7.1 \pm 0.1$ km/s and $V_s = 4.0 \pm 0.1$ km/s, respectively (corrected to room temperature and the pressure of 600 MPa; Rudnick and Fountain, 1995). These results suggest that seismic velocity is higher in the lower crust than in the middle crust, which is consistent with the fact that amphibole abundance is larger in the lower crust than in the middle crust (e.g. Rudnick and Fountain, 1995).

On the other hand, seismic velocity (corrected to room temperature and the pressure of 600 MPa) can be different depending on geological setting. For example, shields and platforms represents high seismic velocity. In particular, seismic velocity in Archean Superior province represented $V_p = 6.80$ km/s and $V_s = 3.90$ km/s in the middle crust; $V_p = 7.24$ and $V_s = 4.13$ km/s in the lower crust (Boland and Ellis, 1991). Grad and Luosto (1987) also showed high seismic velocity in Baltic shield for several samples; $V_p = 6.72 - 7.07$

km/s and $V_s = 3.78 - 4.03$ km/s in the middle crust; $V_p = 6.82 - 7.24$ km/s and $V_s = 4.02 - 4.15$ km/s in the lower crust.

In contrast, seismic velocity in extended regions are relatively low. Goodwin and McCarthy (1990) showed that in west central Arizona V_p and V_s were 6.18 and 3.62 km/s, respectively in the middle crust, and V_p and V_s were 6.82 and 3.83 km/s, respectively in the lower crust. In addition, Braile et al (1982) found that in the Snake River plain V_p and V_s were 6.60 and 3.61 km/s, respectively in the middle crust, and V_p and V_s were 7.10 and 3.93 km/s, respectively in the lower crust.

However, seismic velocity in Paleozoic orogens shows the intermediate values. Seismic velocity in the Alpine provinces of the Iberian Peninsula showed $V_p = 6.56$ and $V_s = 3.57$ in the middle crust, and $V_p = 7.04$ km/s and $V_s = 4.01$ km/s in the lower crust (Banda et al., 1981). Seismic velocity in the North Appalachians was $V_p = 6.41$ km/s and $V_s = 3.70$ km/s in the middle crust, and $V_p = 6.79 - 7.09$ km/s and $V_s = 3.93 - 4.10$ km/s in the lower crust (Luetgert et al., 1987).

On the other hand, several studies of the average P-wave velocity in continental arcs observed $V_p = 6.4 \pm 0.1$ km/s in the middle crust and $V_p = 6.9 \pm 0.1$ km/s in the lower crust, which is similar to those in Paleozoic orogens (Rudnick and Fountain, 1995). Leaver et al. (1984) reported that P-wave

velocities in Cascades in the Pacific Northwest were 6.45 and 6.90 km/s in the middle crust and in the lower crust, respectively. Zelt et al. (1993) reported that P-wave velocities in the Coast plutonic belt were 6.80 and 7.03 km/s in the middle crust and in the lower crust, respectively. Valdes et al. (1986) observed that P-wave velocities in the Trans-Mexico volcanic belt were 5.90 and 6.90 km/s in the middle crust and in the lower crust, respectively. In the Northern Honshu (Japan), Iwasaki et al. (1994b) showed $V_p = 6.45$ and 6.95 km/s in the middle crust and in the lower crust, respectively.

Relatively recent studies have shown seismic anisotropy in the deep crust. In the Ivrea Zone (Northern Italy), Barruol and Kern (1996) showed that anisotropies of P- and S-wave velocities (for S waves propagating parallel to the foliation) for the typical lower-crustal sample were $AV_p = 5.5\%$ and $AV_s = 3.6\%$, respectively. In addition, Tatham et al. (2008) showed that anisotropies of P-wave velocity and of S-wave velocity in the typical lower crust (the Scourie dykes in the Central Block of the Lewisian of NW Scotland) at high shear strains (e.g. $\gamma = \sim 10$) were $AV_p = \sim 7\%$ and $AV_s = \sim 7\%$, respectively.

2.2 CPO of amphibole in natural rocks

CPOs of naturally deformed amphibole in previous studies had mostly shown that (100) plane is nearly parallel to the foliation and [001] axes are aligned subparallel to the lineation (e.g. Mainprice and Nicolas, 1989; Siegesmund et al., 1989; Ji et al., 1993; Berger and Stunitz, 1996; Barruol and Kern, 1996; Kern et al., 2001; Diaz Aspiroz et al., 2007; Fig. 1a). Recent studies however, have reported diverse types of CPOs of amphibole. For instance, many studies have shown the CPO of amphibole in which [100] axes and (010) poles form a great circle girdle subnormal to the foliation and to the lineation, and [001] axes are aligned subparallel to the lineation (Imon et al., 2004; Kitamura, 2006; Diaz Aspiroz et al., 2007; Tatham et al., 2008; Llana-Funez and Brown, 2012; Fig. 1b). Diaz Aspiroz et al. (2007) also reported the CPO of amphibole in which (100) plane is nearly parallel to the foliation and (010) poles and [001] axes form a great circle girdle subparallel to the foliation (Fig. 1c). Another CPO pattern in which (100) plane is nearly parallel to the foliation and (010) poles are aligned subparallel to the lineation was shown by Cao et al. (2010) for the porphyroclasts deformed by rigid-body rotation (Fig. 1d).

2.3 Experimental studies on the deformation of amphibolite

Previous experimental studies of amphibolite had focused on mechanical

behavior of amphibole in only uniaxial compression. Riecker and Rooney (1969) proposed that water weakening can be induced at above the temperature of 800 °C and confining pressures of 0.5 to 2 GPa because of dehydration reaction of hornblende above 800 °C. They also argued that this strength decrease of amphibolite was independent of confining pressure. This result was confirmed by Rooney and Riecker (1973) and Rooney et al. (1975). Experimentally deformed amphibole in earlier studies had shown crystal plasticity at a range of P-T conditions. Rooney et al. (1975) observed twinning on ($\bar{1}01$) (C2/m space group) at pressures of 0.5 to 2 GPa and any temperatures below 800 °C, and translation glide on (100)[001]. Dollinger and Blacic (1975) also observed (100)[001] slip system, but not twinning on ($\bar{1}01$) at the pressure of 1 GPa and temperature of 600 to 750 °C. On the other hand, Hacker and Christie (1990) proposed brittle/ductile transition in experimentally deformed amphibolite at the pressures of 0.5 to 1.5 GPa and temperatures of 650 to 950 °C. They showed that synthetic amphibolite was deformed by crystal plasticity at the temperatures above 750 °C and below strain rate $\dot{\epsilon} = 10^{-5} \text{ s}^{-1}$, while natural amphibolite was deformed by brittle processes under all conditions they conducted experiments.

However, no deformation experiments of amphibole in previous studies had been conducted in simple shear which is the dominant deformation mode in

the lithosphere. Furthermore, previous experimental studies of the development of the CPO of amphibole had been limited compared to observations of naturally deformed amphibole.

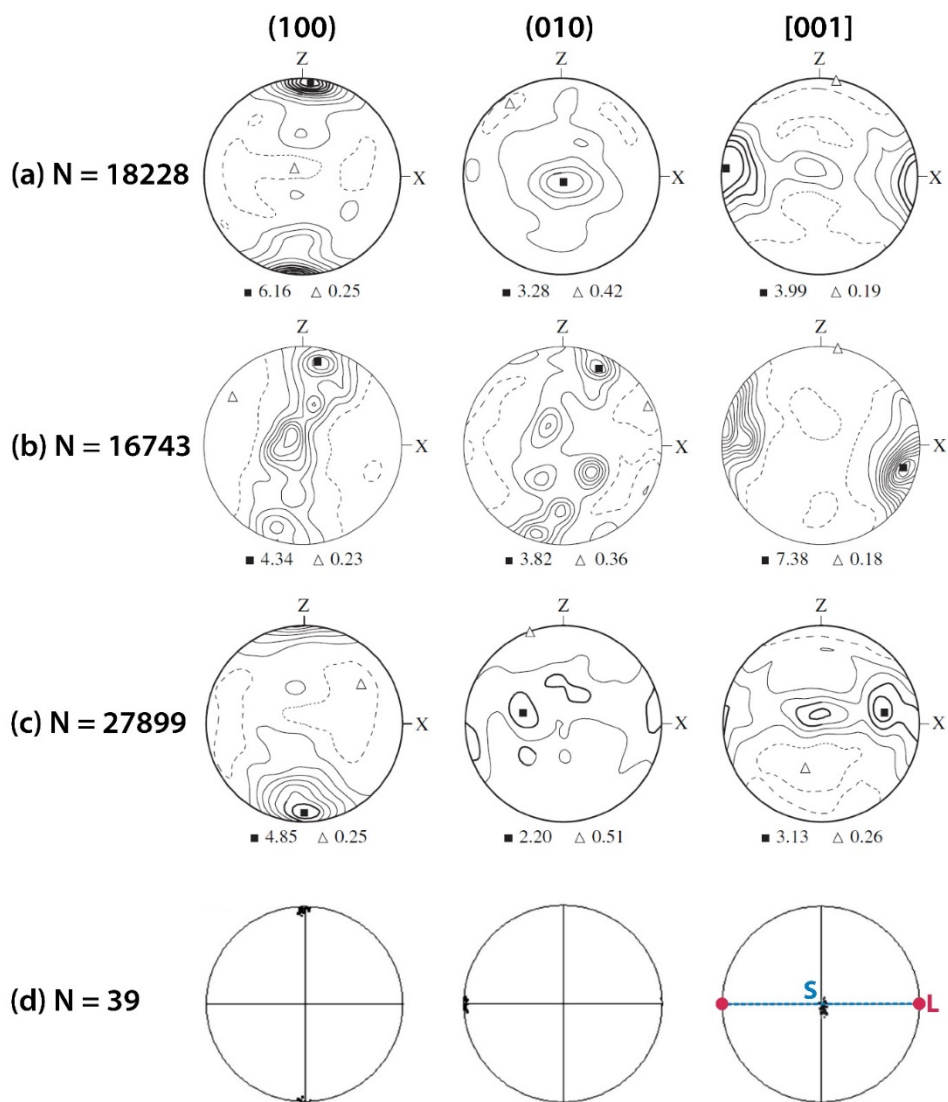


Figure. 1 Pole figures of CPOs of naturally deformed amphibole in previous studies. (a-c) Diaz Aspiroz et al. (2007). X-direction and Z-direction indicate the lineation and foliation normal, respectively. (d) Cao et al. (2010). L-direction and S-plane indicate the lineation and foliation, respectively. “N” indicates measured data points for each CPO.

Chapter 3. Starting material

A natural amphibolite was collected from Yeoncheon in South Korea, which is a massive rock with small grain-size (avg. $\sim 20 \mu\text{m}$) (Figs. 2, 3). The amphibolite is mainly composed of hornblende (68 %), anorthite (23 %), biotite (5 %), titanite (3 %), and ilmenite (1 %). Hornblende in the starting material can be classified as ferro-pargasitic hornblende (Leake, 1978) with the formula of $\text{K}_{1.18}\text{Na}_{0.65}\text{Ca}_{1.9}\text{Mg}_{2.2}\text{Mn}_{0.03}\text{Fe}_{2.0}\text{Ti}_{1.19}\text{Al}_{1.58}(\text{Si}_{6.4}\text{Al}_{1.6})(\text{OH})_2$ (Table 1). Hornblende, which is a common type of amphibole, is the representative mineral at amphibolite facies conditions. The specimen was core – drilled avoiding cracks to cylindrical rods with a diameter of 3.10 mm, and was polished to a thickness of 380 μm after being cut at 45 ° for shear deformation (Fig. 2b). To consider the effect of original fabric (crystallographic preferred orientation) in starting material on the development of new fabric during shear deformation, the CPO of amphibole in starting material was determined before conducting deformation experiments (Fig. 11a).

	Hornblende			Anorthite	Biotite
SiO ₂	43.27	42.39	40.92	54.33	34.43
TiO ₂	1.70	1.54	2.10	0.01	2.93
Al ₂ O ₃	12.40	10.31	11.26	28.61	15.39
Cr ₂ O ₃	0.03	0.00	0.00	0.01	0.00
Fe ₂ O ₃	0.00	0.00	0.00	0.00	0.00
FeO	15.94	16.02	16.43	0.25	18.13
MnO	0.24	0.28	0.31	0.03	0.17
MgO	9.94	10.83	10.05	0.04	12.09
CaO	12.14	12.23	12.14	9.67	0.08
Na ₂ O	2.25	1.77	2.02	6.31	0.39
K ₂ O	0.98	0.90	1.14	0.06	9.49
Total	98.89	96.27	96.37	99.31	93.08

Table 1. The composition of major minerals in the starting material which was determined by EPMA (see Ch.4 Experimental method).

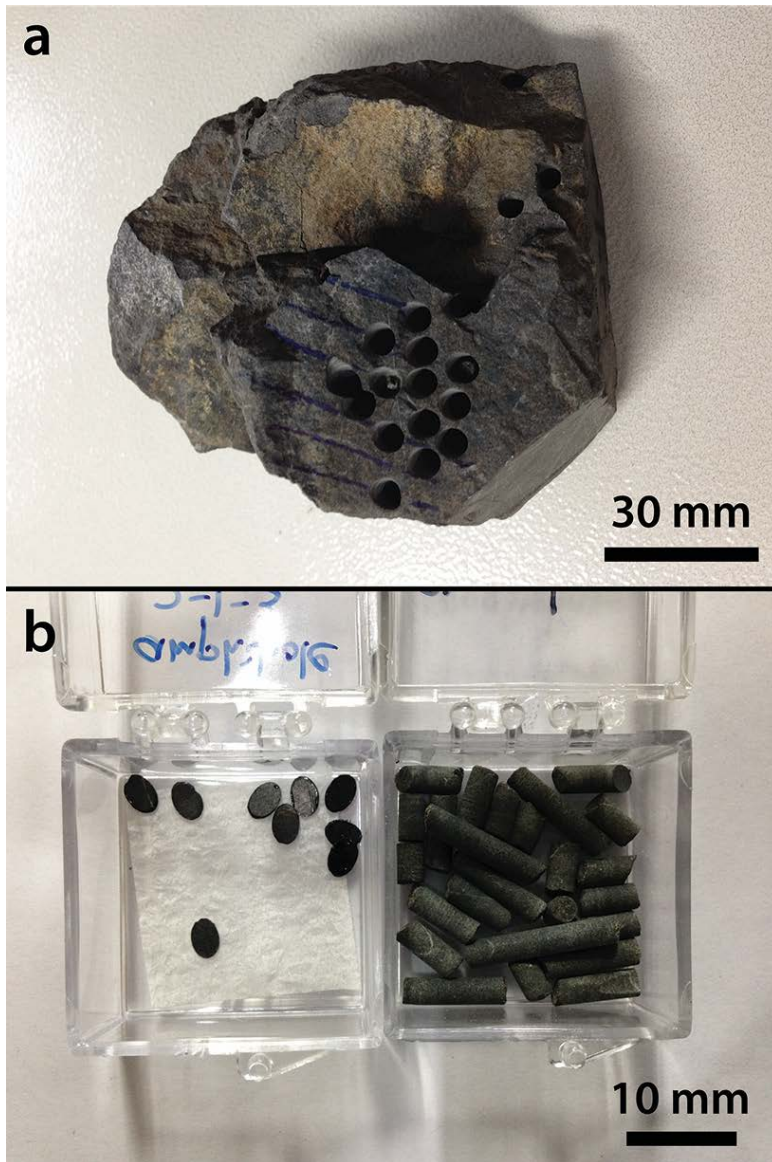


Figure 2. (a) A photograph of the starting material. The amphibolite sample shows many holes that were core-drilled for experiment. (b) The cores of amphibolite (right) and the rock samples cut by 45° to the maximum principle stress for shear experiments (left).

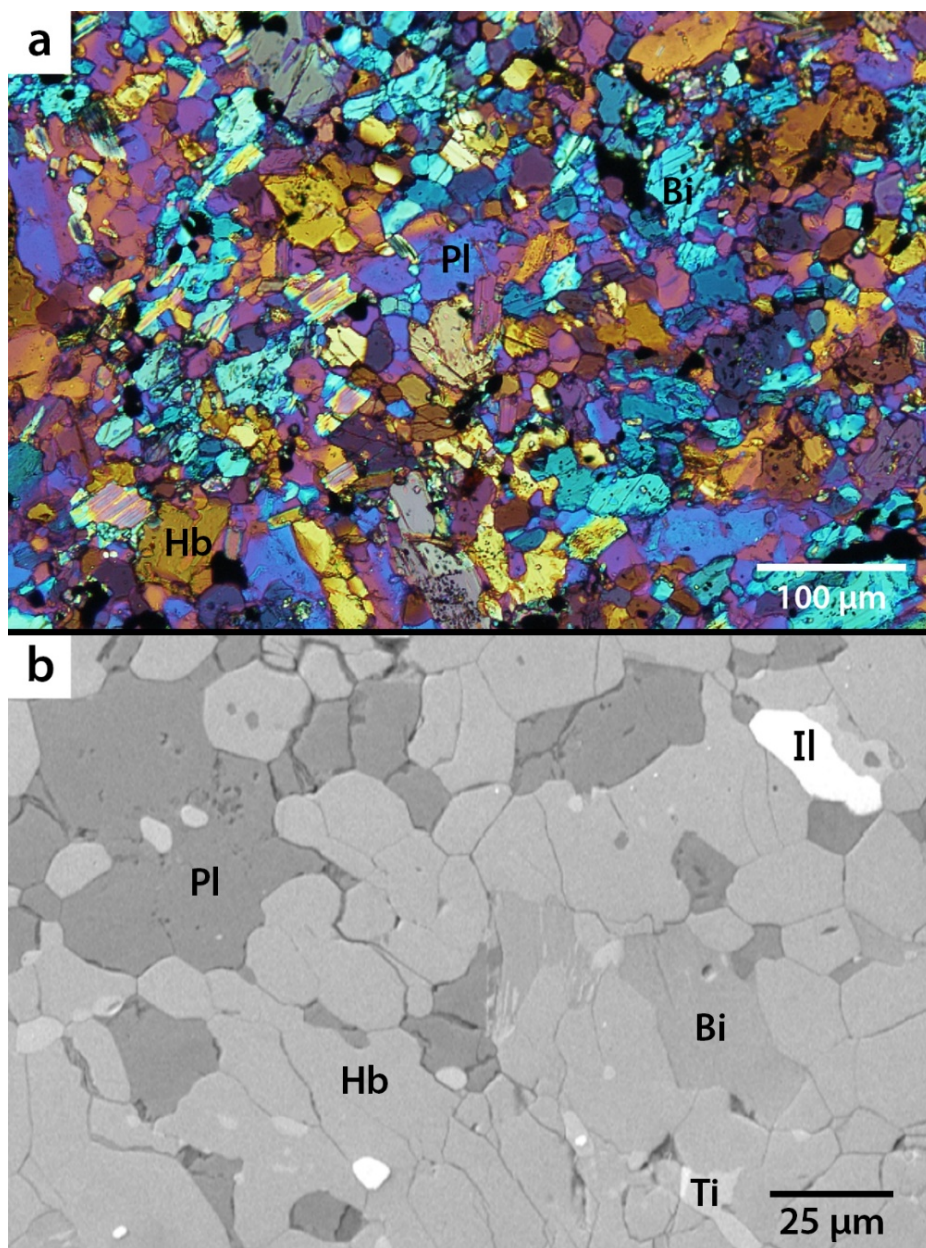


Figure 3. (a) An optical photomicrograph of starting material in cross-polarized light. (b) A backscattered electron (BSE) image of starting material.

Hb: Hornblende, Pl: Plagioclase, Bi: Biotite, Ti: Titanite, Il: Ilmenite.

Chapter 4. Experimental method

4.1 Measurement of sample composition

The composition of constituent minerals were measured by Jeol JXA-8900 electron probe micro analyzer (EPMA) at the National Center for Inter-university Research Facilities in Seoul National University (SNU). The measurement conditions were 15 kV accelerating voltage, 1 nA current, and a beam size of 5 μm . The modal composition of starting material and deformed amphibolite was measured by using the area proportion of each mineral on the 2-dimensional X-Z plane (X: shear direction; Z: shear plane normal). Aggregate boundaries of each mineral were separately traced to calculate areas of each mineral.

4.2 Shear deformation experiment

Deformation experiments of amphibolite were carried out in simple shear at the pressure of 1 GPa and at temperatures of 480 to 700 $^{\circ}\text{C}$ by using a modified Griggs apparatus at SNU. Experimental conditions are shown in Table 2. The amphibolite sample was sandwiched between two alumina pistons cut at 45 $^{\circ}$ to the maximum principal stress inside Ni or Pt jacket under water-poor

condition or water-rich condition, respectively, around which CsCl or NaCl was used as pressure medium (Figs. 4, 5). For experiments under water-rich condition, distilled water (0.03 ± 0.005 g) was pipetted into amphibolite sample in double Pt jacket which can prevent an escape of the water, in order to identify whether the added water influences the development of the CPO of amphibole during deformation. Surfaces of alumina pistons sandwiching amphibolite specimen were carved with several grooves (up to 45 μm depth) to prevent sliding between these pistons and the sample. Shear strain was determined by a rotation of nickel strain marker placed in the middle of the sample with a direction normal to the shear plane (Figs. 5, 8). Stress was measured by external load cell. Temperature was monitored by two thermocouples (70 % Pt 30 % Rh and 94 % Pt 6 % Rh) which are placed close to the Ni or Pt jacket containing the amphibolite specimen. All parts of the sample assembly including starting material had been dried in oven at 120 °C for 6 hours before deformation experiments (see Fig. 6).

Confining pressure was raised for over 10 hours (up to 100 MPa / hr) and temperature was raised within 1 hour (up to 20 °C / min). After reaching desired pressure and temperature, the sample was annealed at least for 1 hour to remove possible defects generated during pressurization. Shear stress was applied to the sample by moving down alumina (Al_2O_3) piston with a constant strain rate. Shear strain rate was in the range of $2.2 \times 10^{-4} \text{ s}^{-1}$ to $1.7 \times 10^{-5} \text{ s}^{-1}$.

The sample was quenched after deformation experiments by turning off electric power to preserve the deformation microstructure, and then pressure was lowered over 12 hours. Shear strain which was measured by the rotation of the nickel strain marker and the elongation of grains was $\gamma = 0.9 - 5.7$.

4.3 Observation of specimen using BSE image

After deformation experiment, sample assembly was recovered and disassembled to take out the nickel or platinum jacket containing the deformed sample. The nickel or platinum jacket was cut along σ_1 by using a low-speed saw, and was impregnated with epoxy. The surface of the sample was polished using a colloidal silica (0.05 μm). After polishing, we coated the surface of the sample with carbon to prevent charging in scanning electron microscope (SEM). Back scattered electron (BSE) images were taken to observe microstructures in deformed samples. JEOL JSM-6380 SEM was employed. Accelerating voltage was 20 kV and working distance was 15 mm.

4.4 Measurement of CPO and calculation of seismic anisotropy

CPOs of amphibole in the deformed sample was determined by using electron

backscattered diffraction (EBSD) with HKL system with Channel 5 software. Accelerating voltage was 20 kV, and working distance was 15 mm in the SEM. The EBSD pattern was indexed manually to ensure an accurate solution at each point. CPOs of hornblende were measured in the sheared sample area where shear strain was homogeneous.

Seismic velocity and seismic anisotropy were calculated from the CPO data of the hornblende with the elastic constants of hornblende (Aleksandrov and Ryzhova, 1961) and a FORTRAN program (Mainprice, 1990). Anisotropy of P-wave velocity (AV_p) was calculated as $[(V_{max} - V_{min}) / ((V_{max} + V_{min})^{0.5})] * 100$, where V is P-wave velocity (V_p). Anisotropy of S-wave velocity (AV_s) was calculated as $[(V_{s1} - V_{s2}) / ((V_{s1} + V_{s2})^{0.5})] * 100$, where V_{s1} and V_{s2} are the fast and slow shear wave velocities, respectively.

Run no.	Temperature (°C)	Shear strain (γ)	Strain rate (s ⁻¹)	Differential Stress (MPa)	Water	Fabric type	Compressional strain (%)
JH54	480 ± 20	1.7 ± 0.8	5.0 × 10 ⁻⁵	192 ± 20	dry	I	27.9
JH53	500 ± 20	1.0 ± 0.1	5.8 × 10 ⁻⁵	150 ± 30	dry	I	17.6
JH65	500 ± 10	5.1 ± 2.0	7.2 × 10 ⁻⁵	53 ± 5	wet ^b	I	52.1
JH75	550 ± 15	1.5 ± 0.9	1.3 × 10 ⁻⁴	39 ± 5	wet	I	41.3
JH40	590 ± 20	4.2 ± 2.1	2.2 × 10 ⁻⁴	261 ± 20	dry	II	34.7
JH46	600 ± 15	2.9 ± 1.6	3.6 × 10 ⁻⁵	113 ± 10	dry	II	40.8
JH58	600 ± 15	1.8 ± 1.1	4.4 × 10 ⁻⁵	155 ± 15	dry	II	21.1
JH62	600 ± 20	1.5 ± 0.2	4.0 × 10 ⁻⁵	59 ± 5	wet	I	24.2
JH72	600 ± 10	2.2 ± 0.3	6.0 × 10 ⁻⁵	49 ± 5	wet	I	35.0
JH74 ^a	640 ± 15	3.1 ± 0.6	>1.1 × 10 ⁻⁴	67 ± 5	wet	III	47.4
JH49	650 ± 15	5.7 ± 0.5	2.2 × 10 ⁻⁴	132 ± 10	dry	II	43.7
JH56	690 ± 15	3.5 ± 0.4	7.6 × 10 ⁻⁵	128 ± 10	dry	III	31.6
JH64	690 ± 20	0.9 ± 0.7	1.7 × 10 ⁻⁵	34 ± 5	wet	III	29.7
JH43	700 ± 10	1.5 ± 0.6	1.4 × 10 ⁻⁴	170 ± 20	dry	II	34.2

Table 2. Experimental conditions and results. All experiments were conducted at the pressure of 1 GPa.

^aShear strain of JH74 was measured by elongated plagioclase grains because strain marker was missing. For other samples, shear strain was determined by the rotation of Ni strain marker.

^bFor wet experiments, water (0.03±0.005 g) was added into the specimen (see Ch.4.2 Shear deformation experiment).

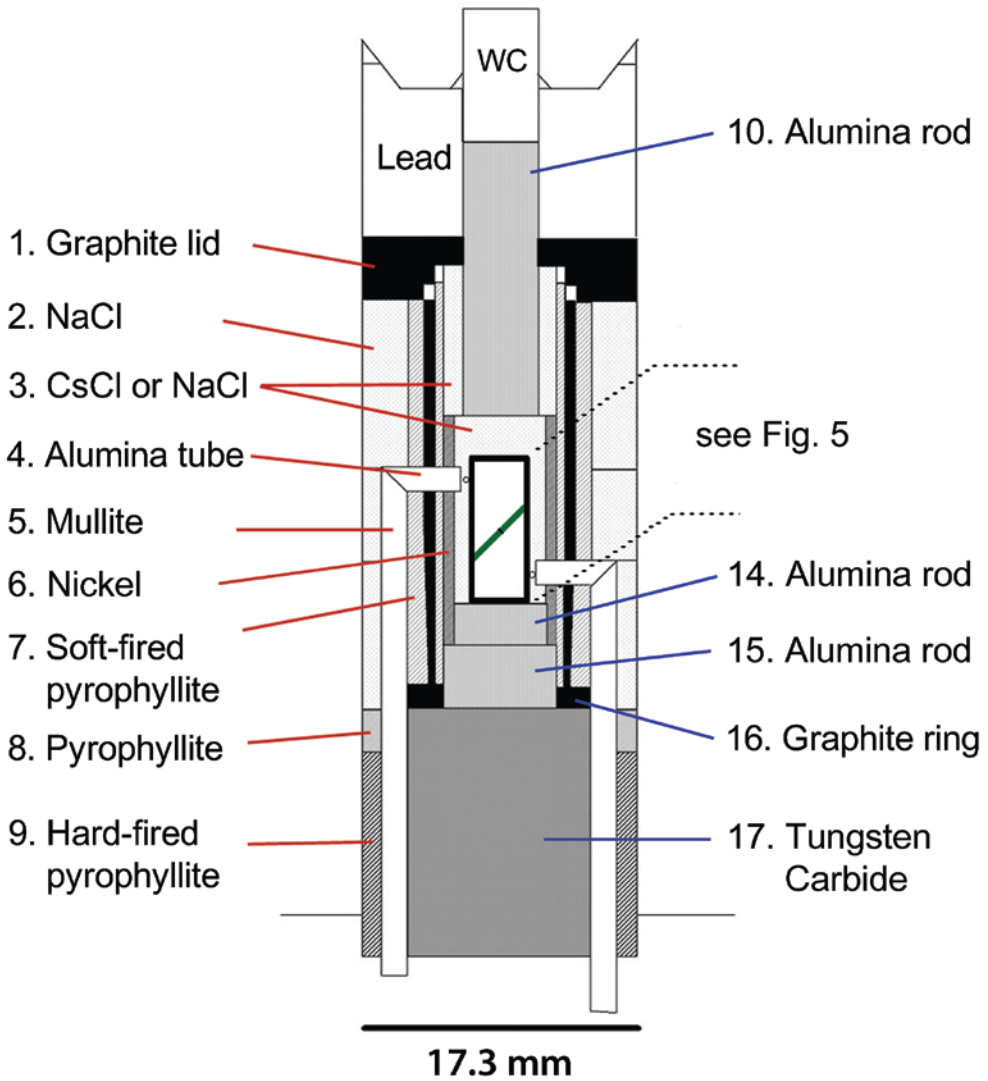


Figure 4. A schematic figure showing the sample assembly for shear deformation experiment at high pressure and temperature. The center part is described in detail in Fig. 5. WC: Tungsten Carbide. Numbering corresponds to that of Fig. 6.

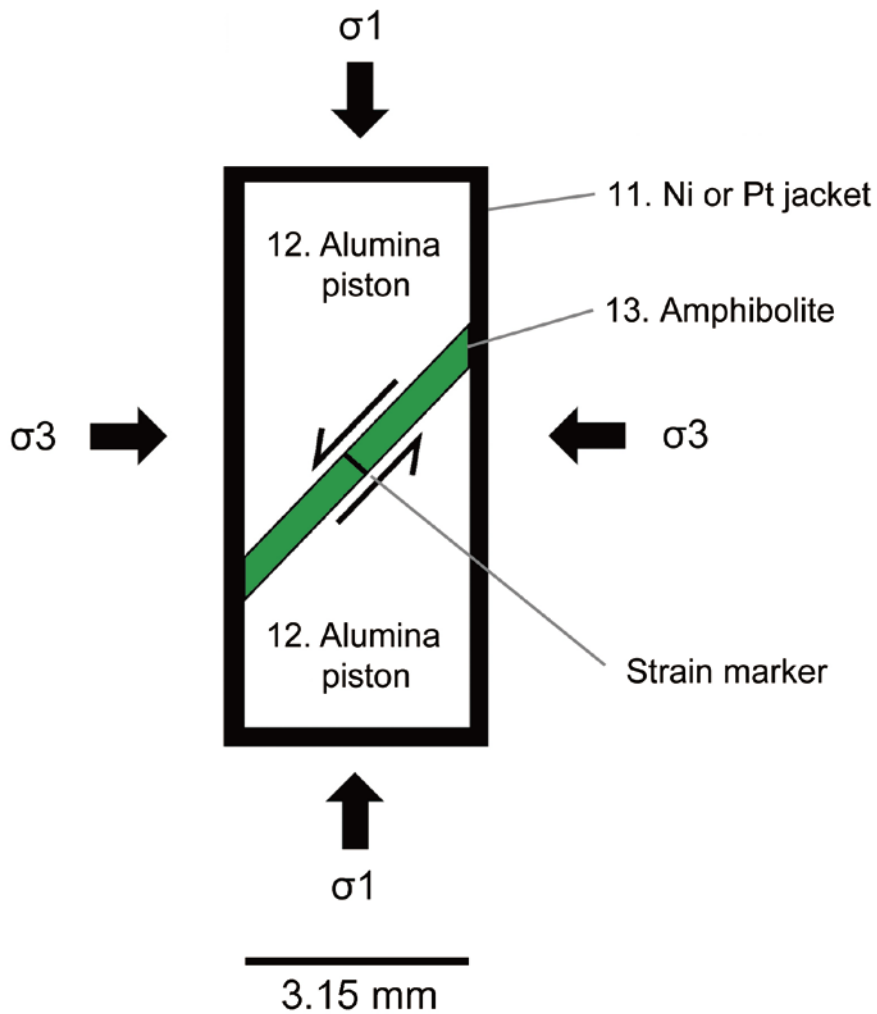


Figure 5. A schematic figure showing the central part of sample assembly. Amphibolite sample was placed inside Ni or Pt jacket. Sample is sandwiched between two alumina pistons cut by 45° to the maximum principle stress (σ_1). Strain marker (Ni) was placed perpendicular to shear plane in the middle of the sample.

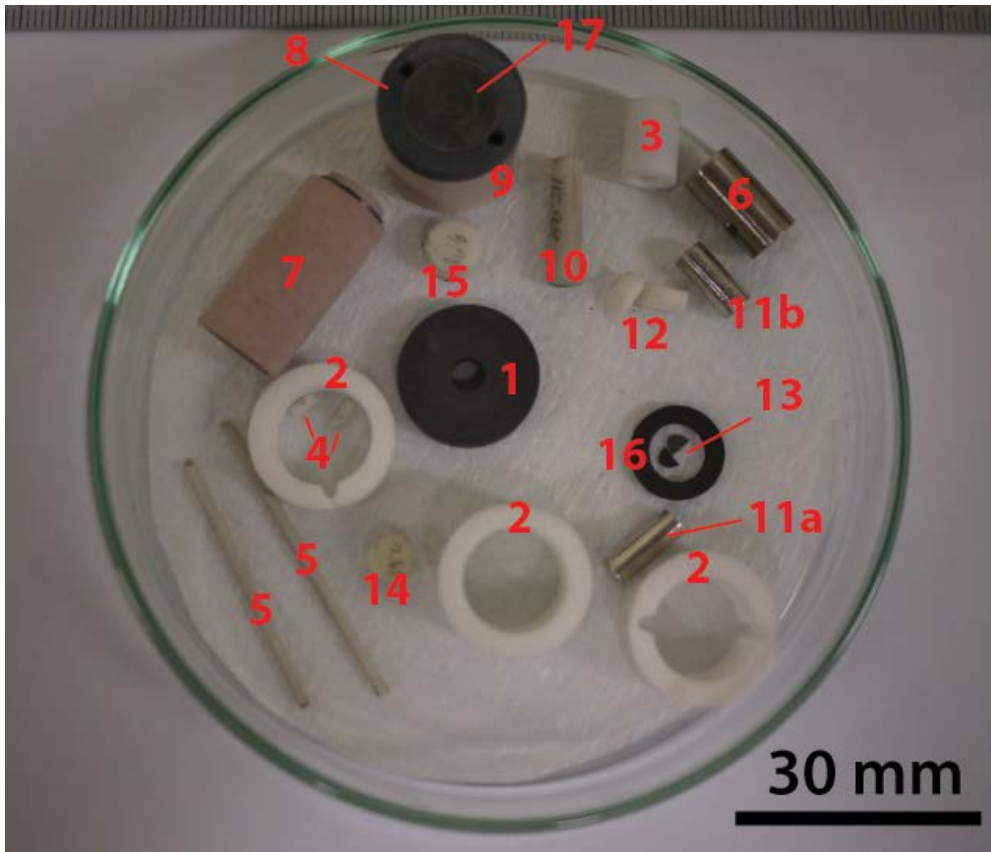


Figure 6. Parts of sample assembly used in the experiment (JH72). 1: Graphite lid, 2: NaCl ring, 3: CsCl or NaCl, 4: Alumina tube, 5: Mullite, 6: Nickel, 7: Furnace set, 8: Pyrophyllite, 9: Hard-fired pyrophyllite, 10: Alumina rod (16 mm long), 11a: Pt inner capsule, 11b: Pt outer capsule, 12: Alumina pistons cut by 45 °, 13: Amphibolite specimen, 14: Alumina rod (2.54 mm long), 15: Alumina rod (3.84 mm long), 16: Graphite ring, and 17: Tungsten Carbide.

Chapter 5. Results

The CPO of starting material is described in Fig. 11a. The CPO pattern of starting material is relatively random with low maximum m.u.d. value ~ 2 . [001] axes are clustered in the west side of the upper part in the pole figure, which is not shown in CPOs of deformed amphibole in this study. Modal composition of a deformed amphibolite (JH74) was Hb = 74 %, An = 17 %, and other minerals = 9 % which is not much different from that of starting material (Hb = 68 %, An = 23 %, and other minerals = 9 %).

5.1 Mechanical data

Experimental results are shown in Table 2. Differential stress ($\sigma_1 - \sigma_3$) of deformed samples at high pressure and temperature was sensitive to existence of added water (Fig. 7). Differential stress of deformed amphibolite in wet condition was only $\sim 30 - 50$ % of that in dry condition at the same temperature and strain rate.

5.2 Microstructures

The thickness of deformed samples was reduced by 34 % on average after

deformation (Table 2). Microstructures in all deformed samples showed about the same brittle structure. BSE images in Figs. 8 – 10 represent that faults and microcracks were mostly formed in deformed samples and that the grain shape is angular with the very fine grain size ($< 5 \mu\text{m}$). Another major feature is the strong strain localization in any scales from mm to μm , which is intimately related to the generation of faults and the comminution of grains. The localized shear zone was developed after $\gamma \sim 0.8$ around the main faults produced at $0 - 30^\circ$ to the shear plane (Fig. 8). Macroscopically, plagioclase seems to appear plastic deformation owing to an elongated structure of plagioclase aggregates that are subparallel to rotated strain markers. In contrary, microscopic observations reflect cracking feature, indicating that plagioclase was deformed by brittle or semi-brittle processes. The observation of severe grain size reduction and microfracturing in deformed amphibolites imply that the dominant deformation mechanism was cataclastic flow with faulting accompanied by the rotation of hornblende grains in the weaker plagioclase matrix. The more detailed analysis on the deformation mechanism will be discussed in Ch. 6.1 Deformation mechanism.

5.3 CPOs of amphibole

Three fabric types (Type-I, -II, and -III) of hornblende were found (Fig. 11) after deformation experiment in simple shear, all of which displays that (100) poles are aligned subnormal to the shear plane. Obtained fabrics in deformed hornblende are clearly distinct from the fabric in starting material. Typical CPO types in this study are displayed in Fig. 18. Type-I fabric represents that [001] axes are aligned subparallel to the shear direction. Type-II fabric represents that (010) poles are aligned subparallel to the shear direction. Type-III fabric shows that (010) poles and [001] axes form a great circle girdle subparallel to the shear plane.

5.4 Seismic anisotropy

Seismic velocities and seismic anisotropies corresponding to each fabric type of the deformed amphibole are illustrated in Figs. 12 – 16. P- and S-wave velocities (V_p and V_s , respectively) show the relation with the orientation of three different principal axes of hornblende. The location of the minimum P-wave velocity of all fabric types (I, II, and III) in horizontal flow, for example (Fig. 12), is near the center of the figure, which corresponds to the orientation of the maximum density of (100) poles in pole figure since a-axis is the slowest axis in hornblende axes.

The location of the maximum P-wave velocity varies depending on fabric types. The maximum P-wave velocity of type-I fabric in horizontal flow corresponds to the orientation of the maximum density of [001] axes in pole figure which is the fastest axis in hornblende axes, whereas that of type-II and -III fabrics is distributed regardless of the orientation of the maximum density of [001] axes. On the other hand, the location of the maximum S-wave velocity of all three fabric types in horizontal flow mostly correspond to the orientation of the maximum density of [001] axes.

Anisotropies of P-wave velocity (AV_p) and S-wave velocity (AV_s) were in the range of 9.0 – 14.6 % and 7.63 – 12.96 %, respectively (Table 2).

Seismic anisotropies illustrate different directions of the polarized fast shear wave (V_{s1} polarization) depending on flow geometry. In horizontal flow in which the center of the stereonet (z) corresponds to the direction normal to horizontal shear plane, and shear direction (x) corresponds to the E-W direction, V_{s1} polarization direction is different for each fabric type (Fig. 12). For type-I fabric, V_{s1} polarization direction tends to be subnormal to the shear direction at the center of pole figure, while for type-II fabric, it tends to be subparallel to the shear direction. For type-III fabric, V_{s1} polarization direction shows either subnormal or subparallel to the shear direction. On the other hand, for the flow dipping at 30° and 45° from the horizontal flow, V_{s1}

polarization direction tends to be nearly normal to the shear direction regardless of three fabric types (Figs. 13 and 14). Furthermore, in the case of JH75, Vs1 polarization anisotropy for the vertically propagating S-wave dramatically increased up to 5.5 and 8.5 % for $\theta = 30^\circ$ and $\theta = 45^\circ$, respectively, while that in horizontal flow was only 1.0 %. This increase of Vs1 anisotropy at $\theta = 90^\circ$ was up to 12.3 % (JH54) for the vertical shear (Fig. 15; Table 2).

Run no.	Maximum anisotropy		AVs (%) for the flow dipping angle at			
	AVp (%)	AVs (%)	0 °	30 °	45 °	90 °
JH54	12.8	12.1	1.7	5.0	8.6	11.7
JH53	13.0	10.5	1.6	3.3	4.8	5.5
JH65	13.7	11.8	1.5	3.8	7.0	10.6
JH75	13.5	11.1	1.0	5.5	8.5	8.3
JH40	10.6	8.9	2.3	2.0	4.5	6.2
JH46	9.9	9.4	1.4	3.2	5.5	6.6
JH58	14.6	11.5	1.1	3.0	6.5	9.5
JH62	13.5	11.5	1.2	3.3	5.8	10.8
JH72	12.5	9.2	0.9	3.5	5.8	8.3
JH74	12.7	10.6	0.6	3.5	6.0	8.5
JH49	12.7	9.2	0.8	2.0	4.6	6.9
JH56	13.1	11.1	1.1	2.6	6.0	8.9
JH64	13.8	10.4	0.8	3.4	5.4	10.2
JH43	9.0	7.6	2.0	1.8	3.6	4.5

Table 3. Seismic anisotropy calculated from CPOs of amphibole. AVp and AVs indicate anisotropies of P-wave velocity and S-wave velocity, respectively. AVs for the flow dipping at 0, 30, 45, and 90 ° was measured from the center of pole figures for vertically propagating shear wave (see also Figs. 12 – 15).

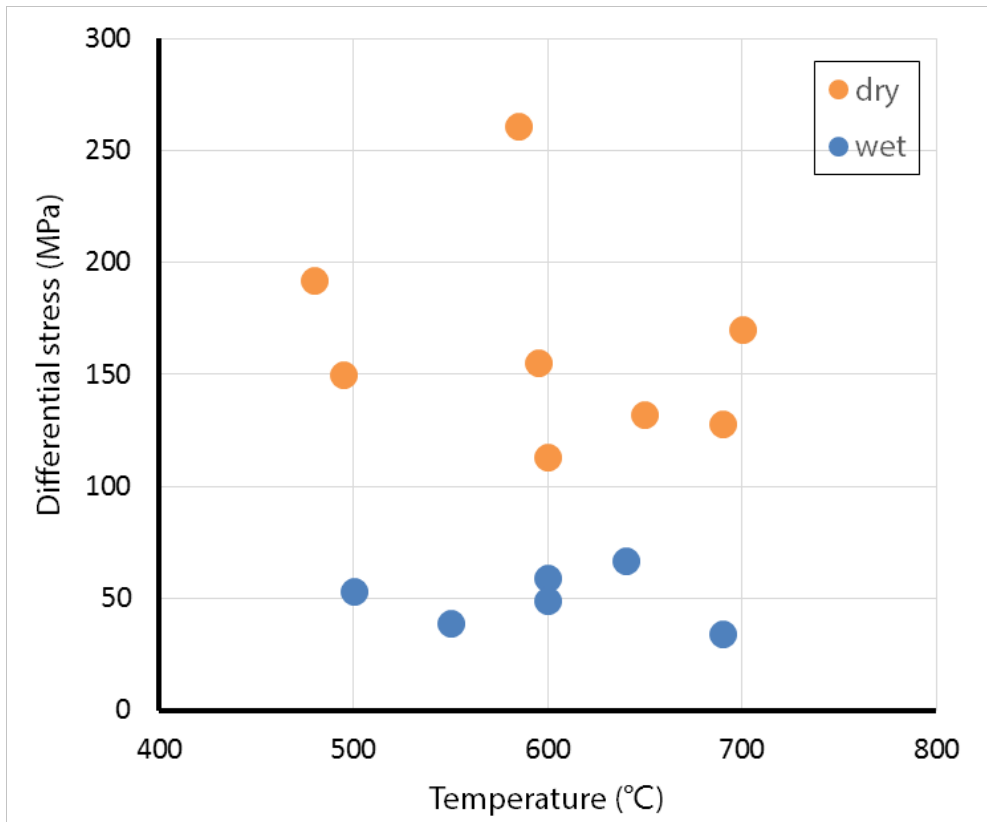


Figure 7. Strength-temperature diagram of deformed amphibolites. Each stress data is measured from the peak value of differential stress after yielding. Blue and orange circles indicate experiments in wet condition and dry condition, respectively.

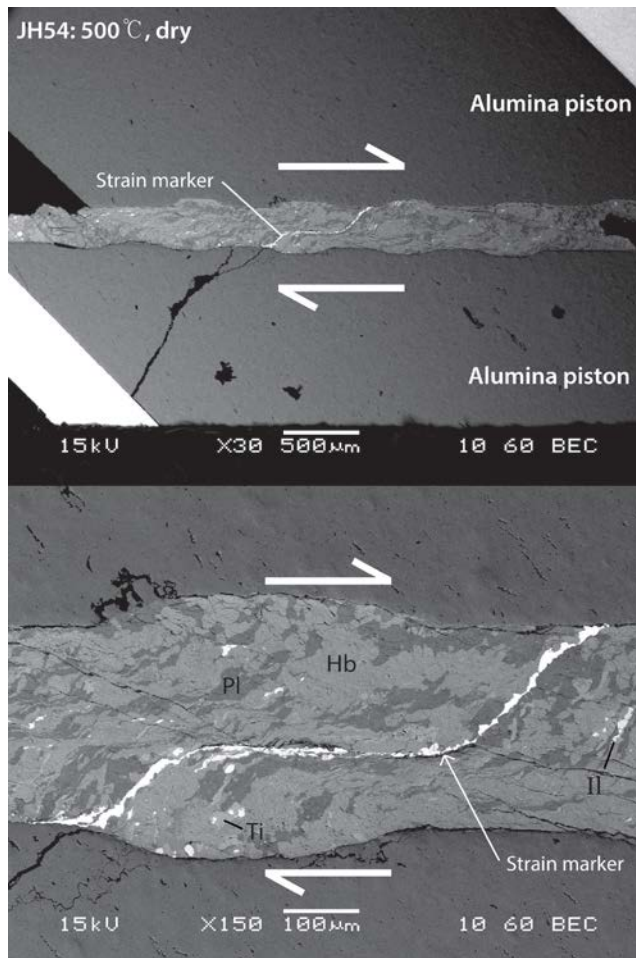


Figure 8. BSE images of deformed amphibolite (JH54). Pressure during deformation was 1 GPa. The bottom image is the magnified view of the central portion of the top image. Arrows indicate shear direction, dextral shear sense. The rotation of strain marker is shown in the center part of images. Strain localization around strain marker is represented with faults penetrating the sample with an angle of $\sim 30^\circ$. Hb: Hornblende, Pl: Plagioclase, Ti: Titanite, Il: Ilmenite.

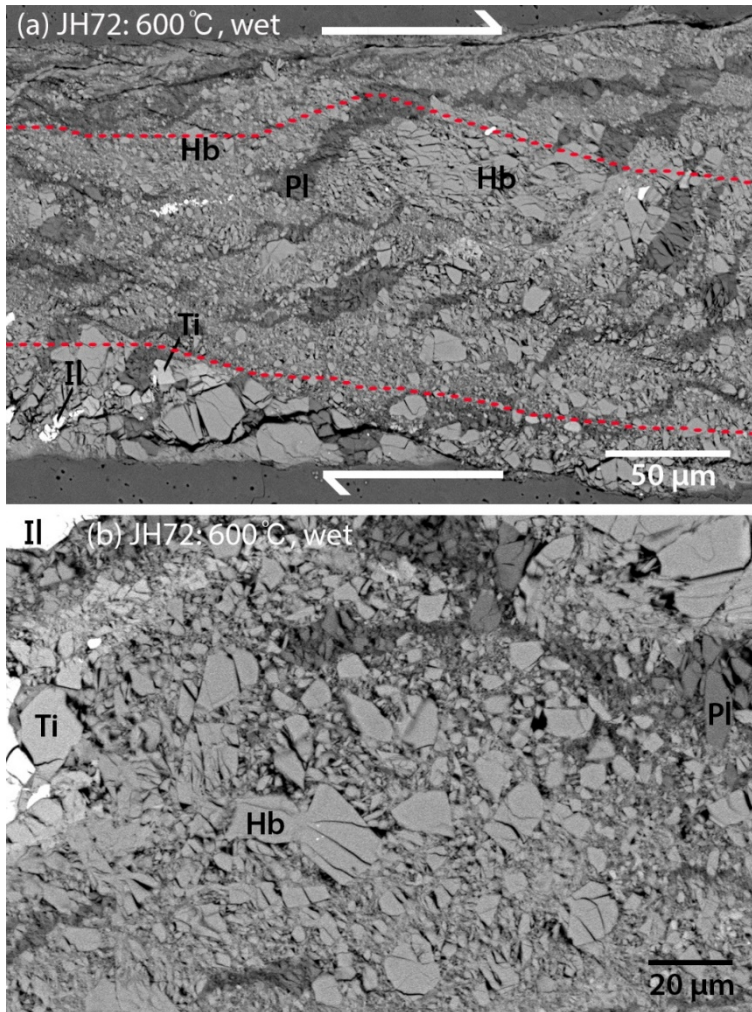


Figure 9. BSE images of (a, b) deformed amphibolite of JH72. Pressure during deformation was 1 GPa. After brittle deformation processes, amphibolite shows smaller grain size, angular grain shape and strain localization with faults. The arrows indicate shear direction, dextral shear sense. CPO of amphibole was measured in the region bounded by two broken red lines. Hb: Hornblende, Pl: Plagioclase, Ti: Titanite, Il: Ilmenite.

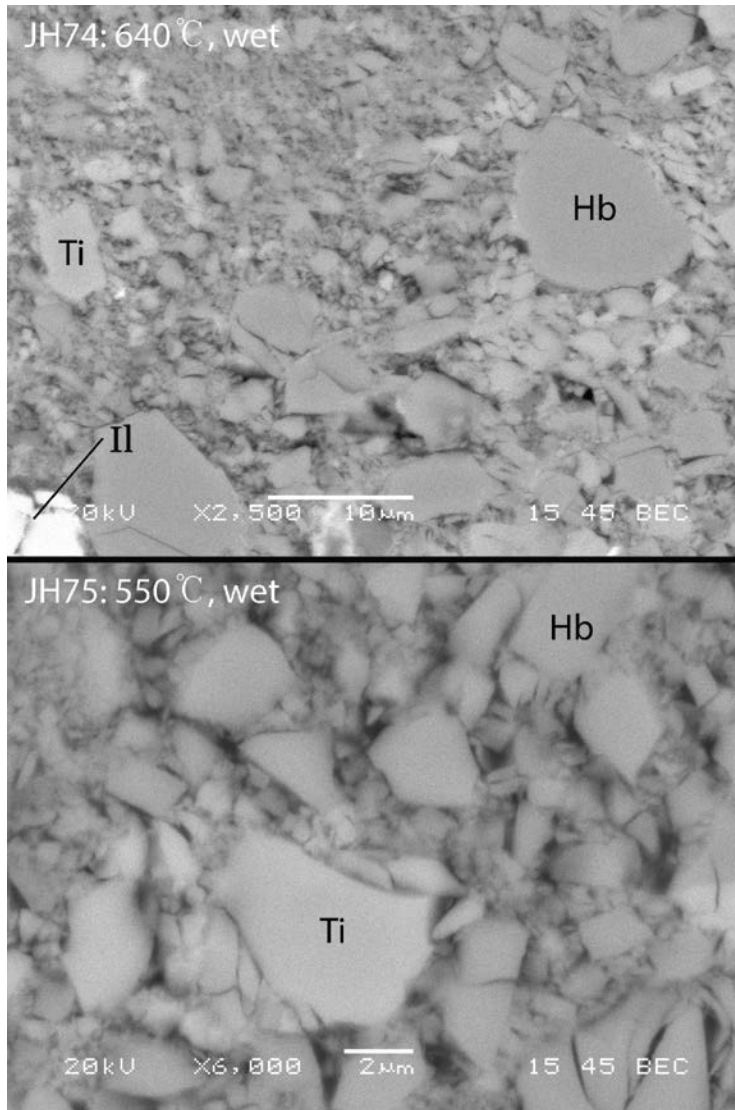


Figure 10. BSE images of deformed amphibolites (JH74, JH75). Pressure during deformation was 1 GPa. Very fine grains are fractured with angular shape. Hb: Hornblende, Ti: Titanite, Il: Ilmenite.

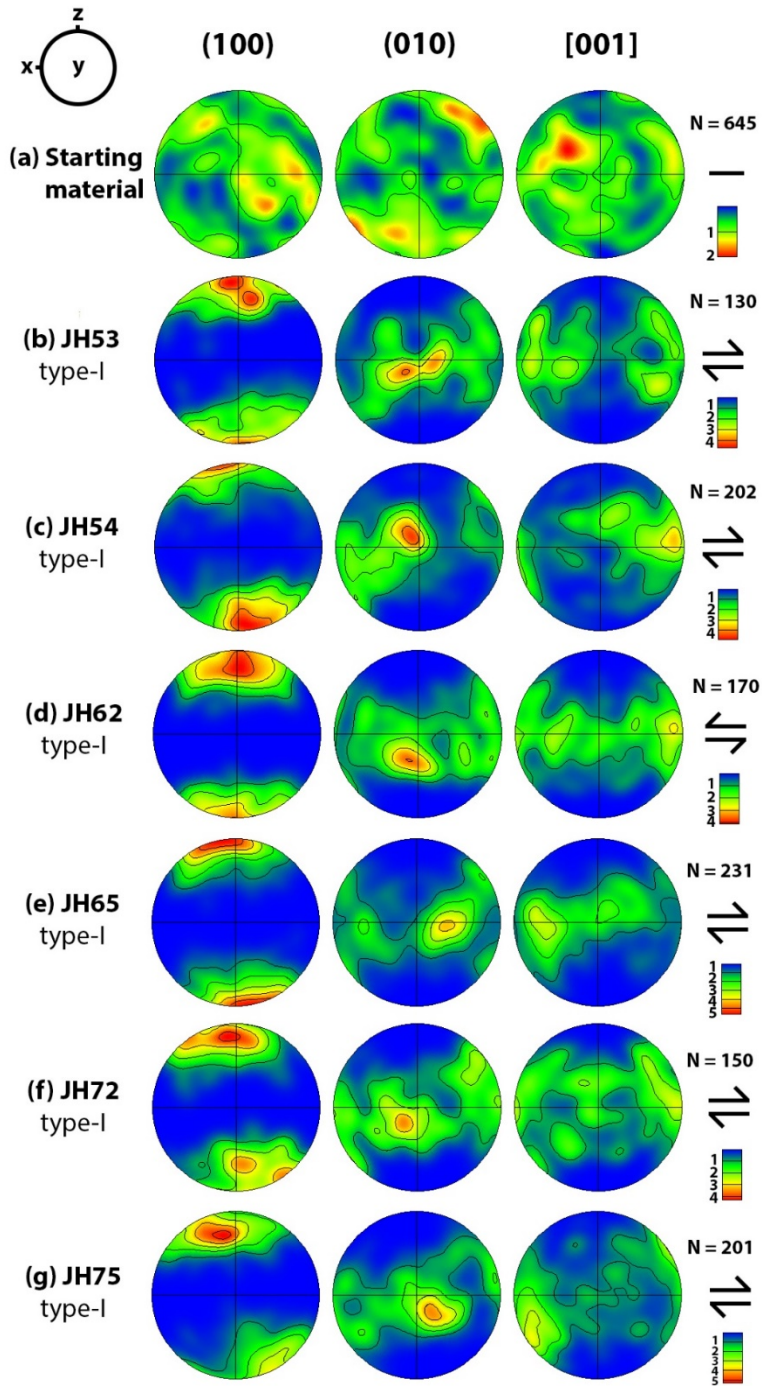


Figure. 11 (Figure caption is in page 34)

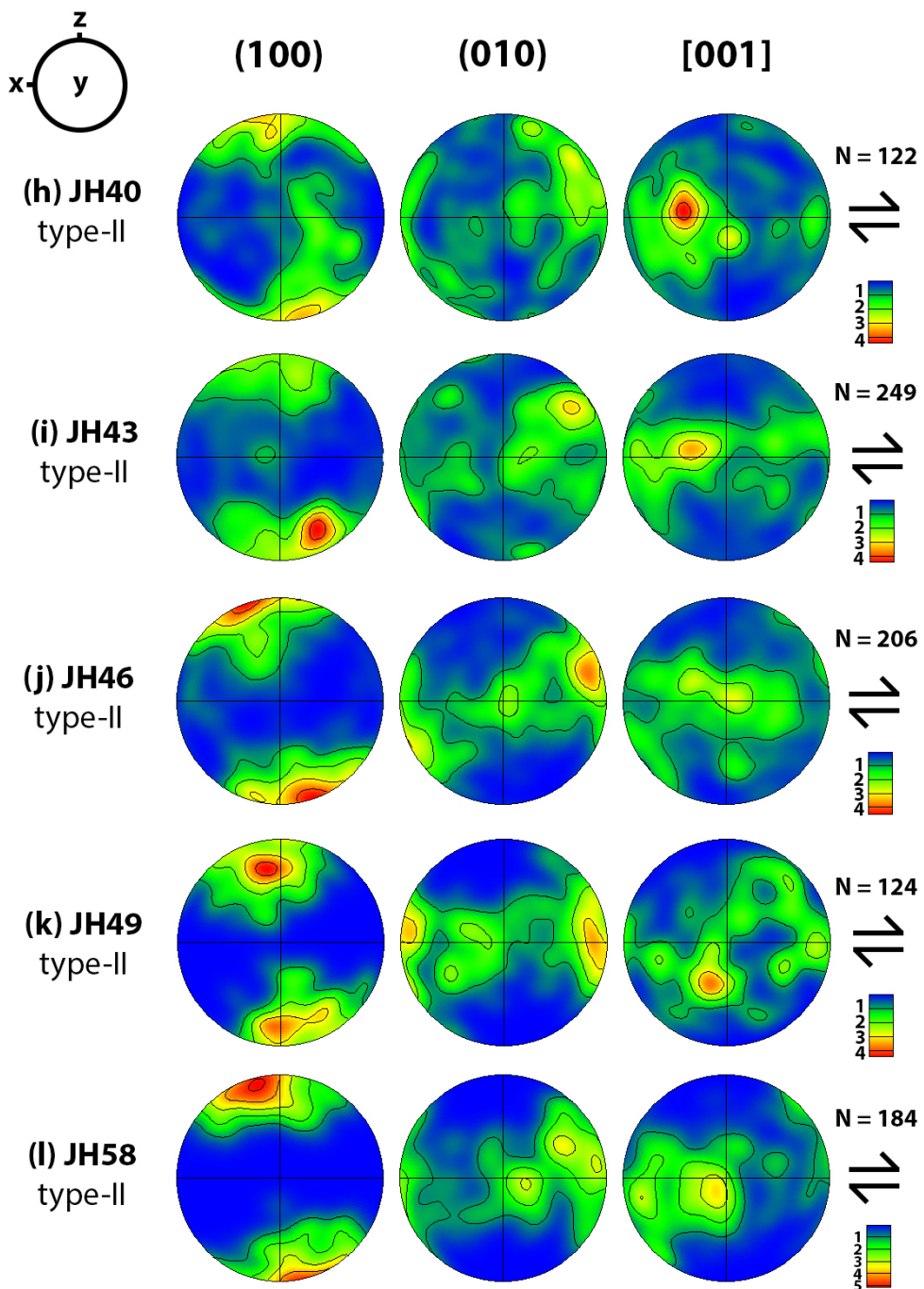


Figure. 11 (Figure caption is in page 34)

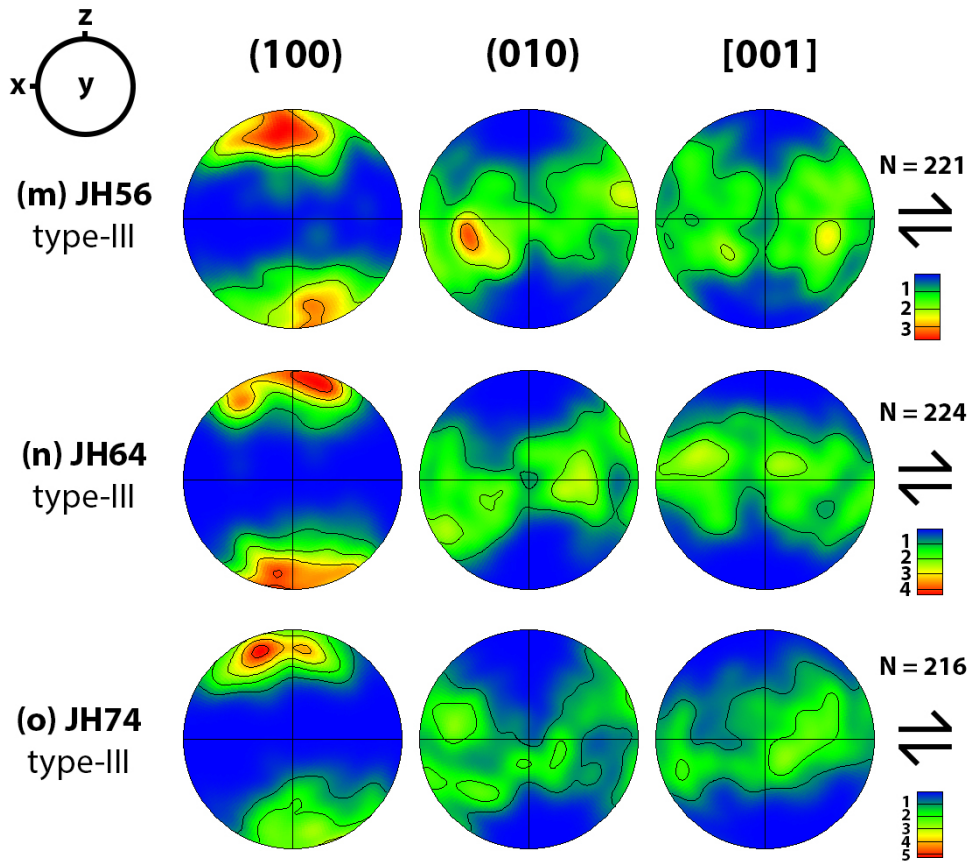


Figure 11. Pole figures of crystallographic preferred orientation (CPO) of deformed amphibole at the pressure of 1 GPa. The X-direction and the Z-direction correspond to the shear direction and the shear plane normal, respectively. The arrows indicate the dextral shear sense. The pole figures are equal-area upper-hemisphere projections with a half-width of 20 °. “N” indicates data points measured in each sample. (a) Original fabric in starting material. (b – g) Type-I fabric. (h – l) Type-II fabric. (m – o) Type-III fabric.

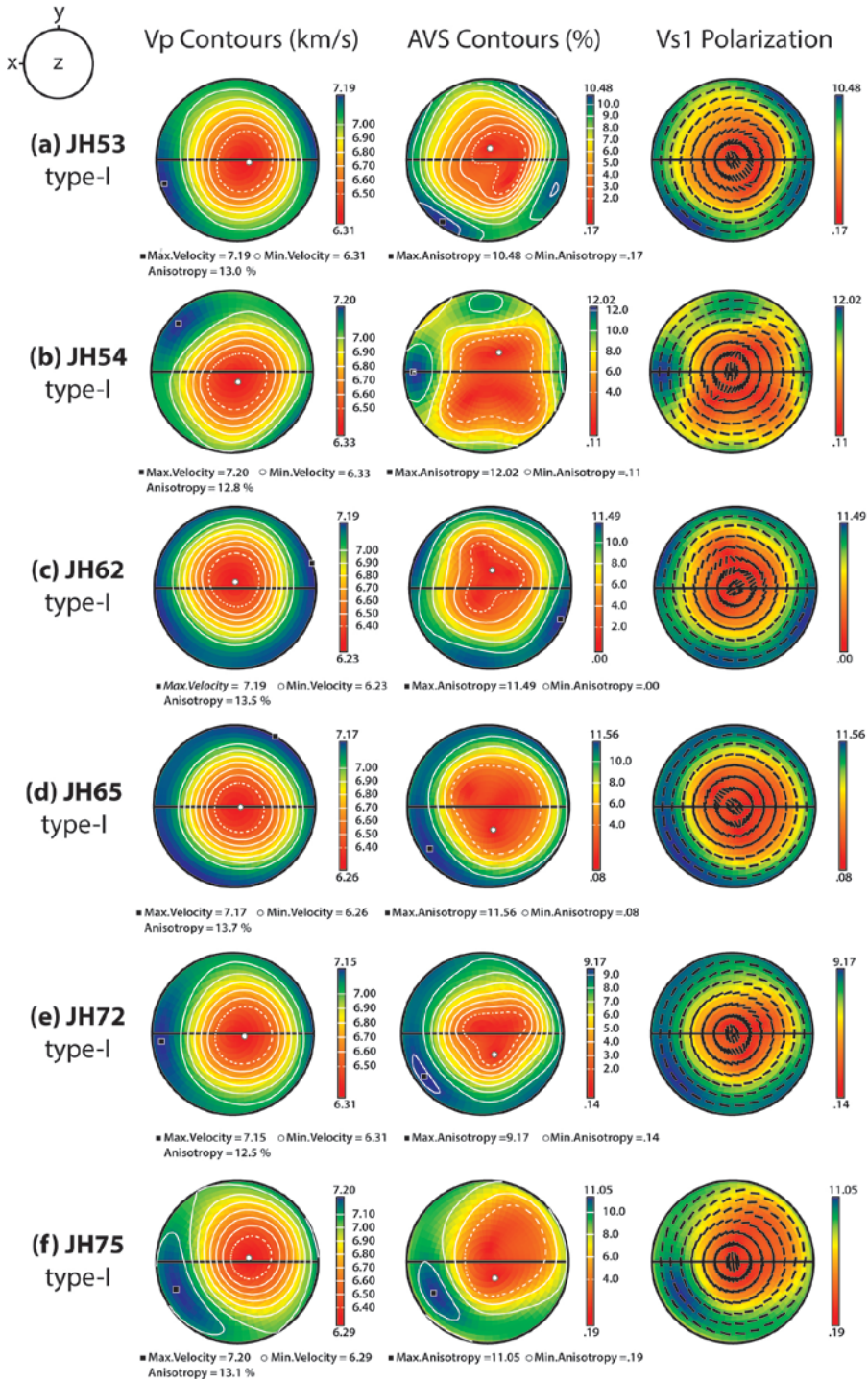


Figure. 12 (Figure caption is in page 37)

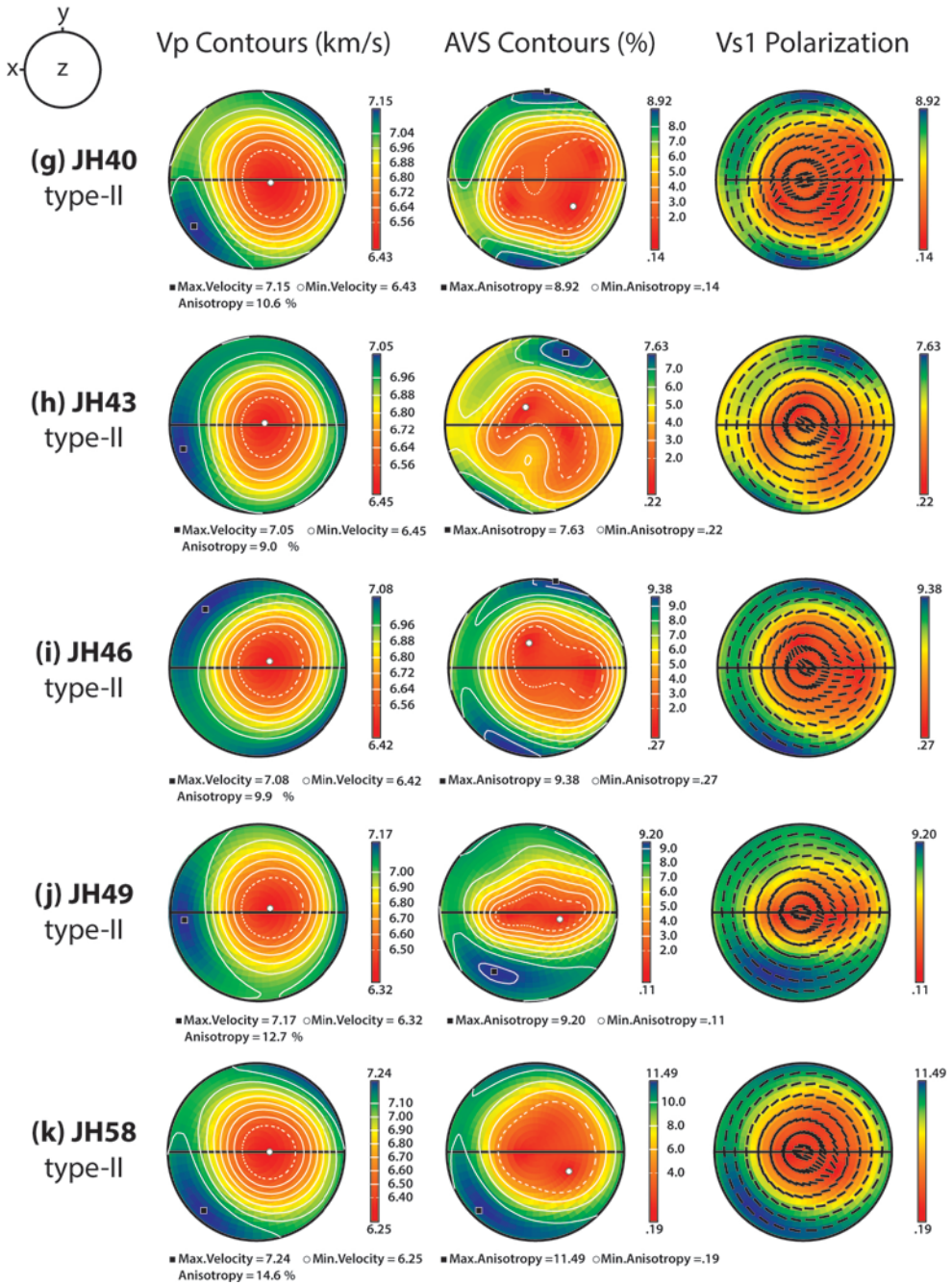


Figure. 12 (Figure caption is in page 37)

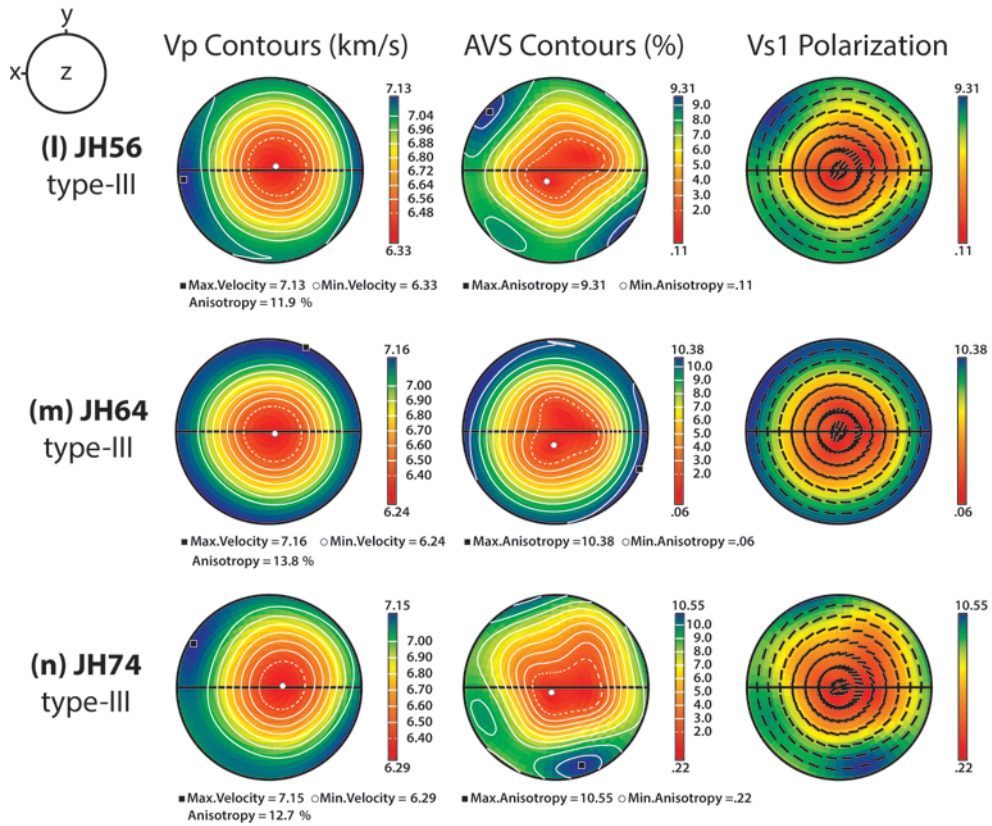


Figure 12. Seismic anisotropy corresponding to the fabrics shown in Fig. 11 in the horizontal flow. Equal area and lower-hemisphere projections were used. The X-direction and the Z-direction correspond to the shear direction and the direction normal to the shear plane, respectively. Center of pole figure of Vs1 polarization represents the direction of vertically propagating S-wave. Type-I fabric shows the direction of the polarized fast shear wave subnormal to the shear direction, whereas type-II fabric represents that subparallel to the shear direction.

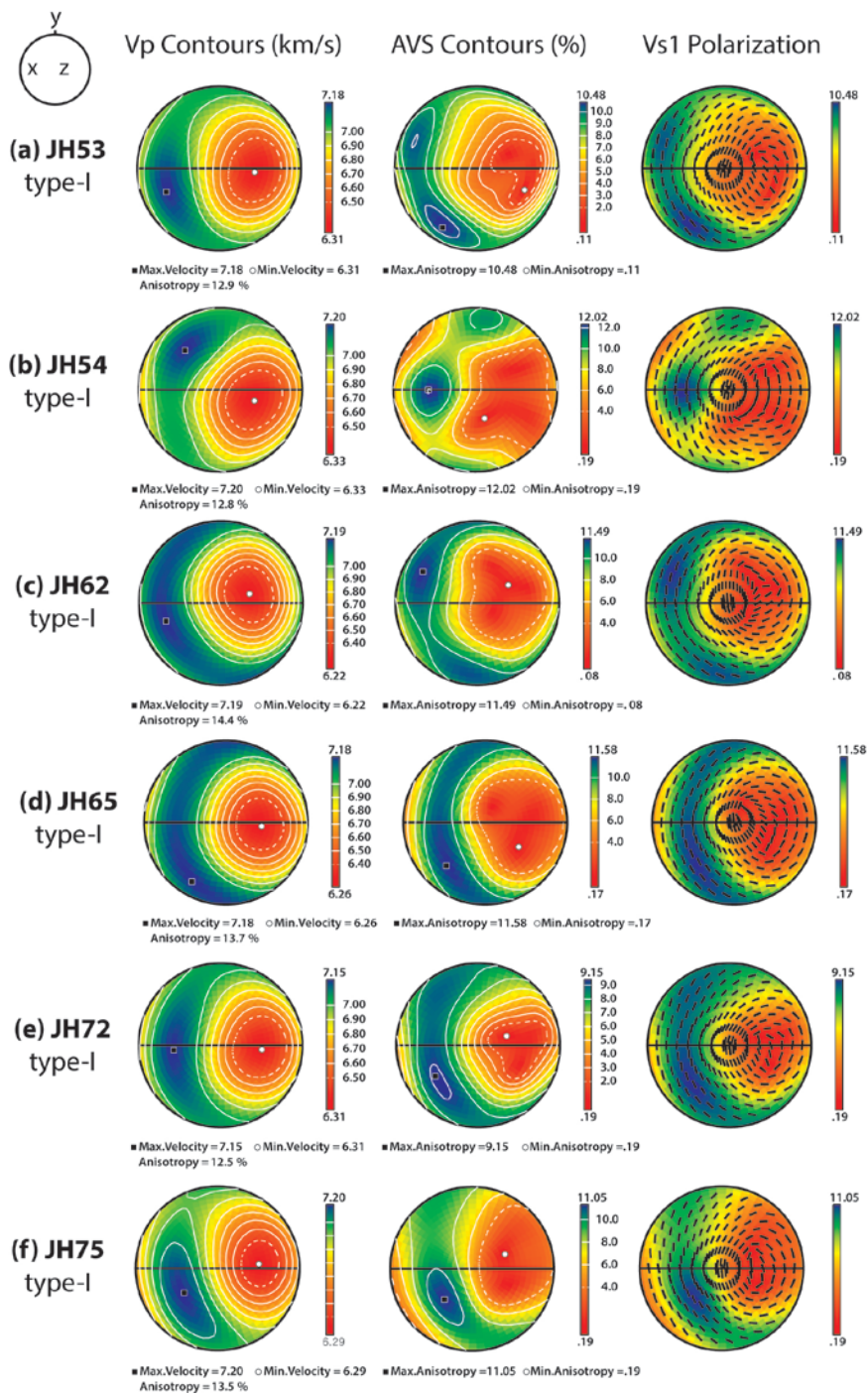


Figure. 13 (Figure caption is in page 40)

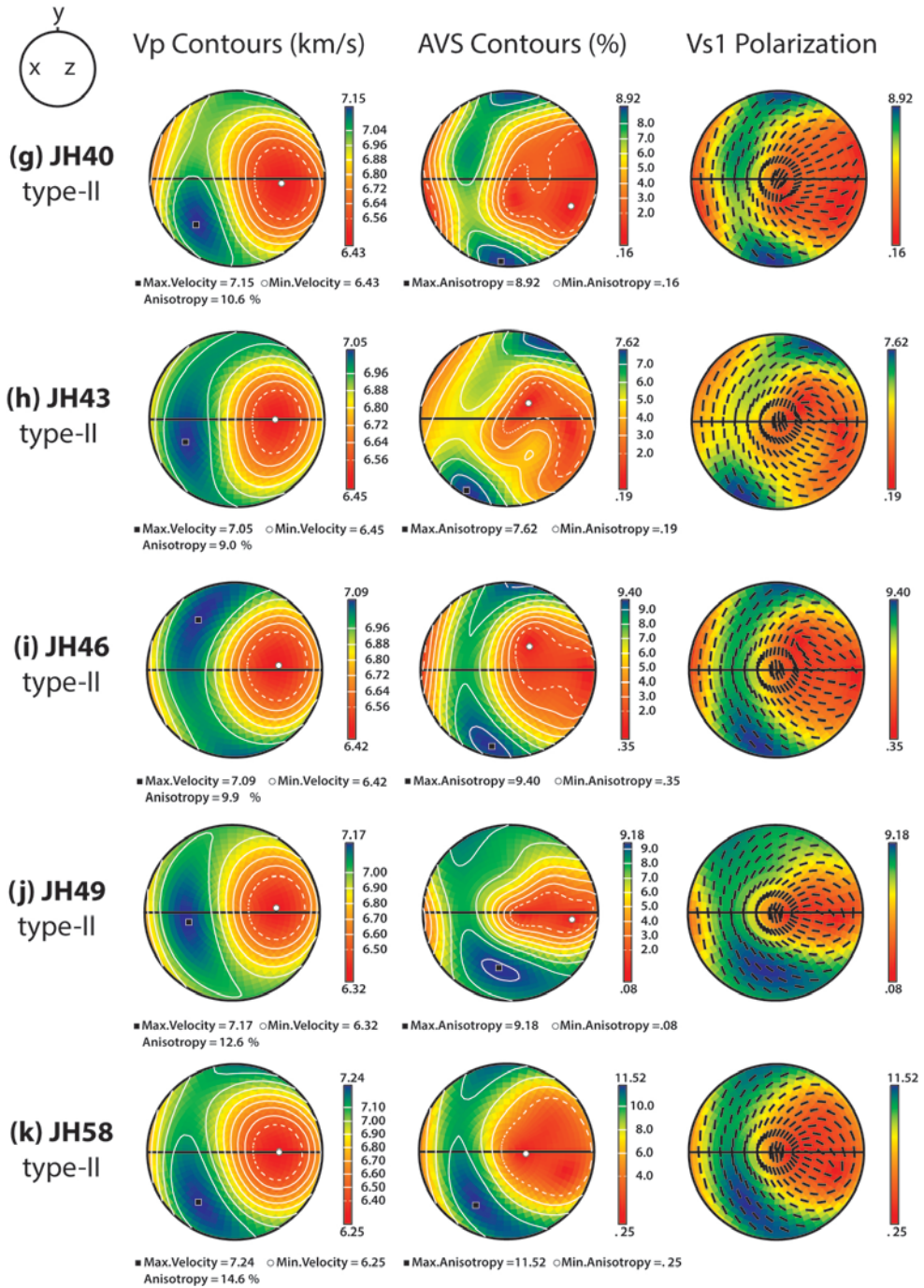


Figure. 13 (Figure caption is in page 40)

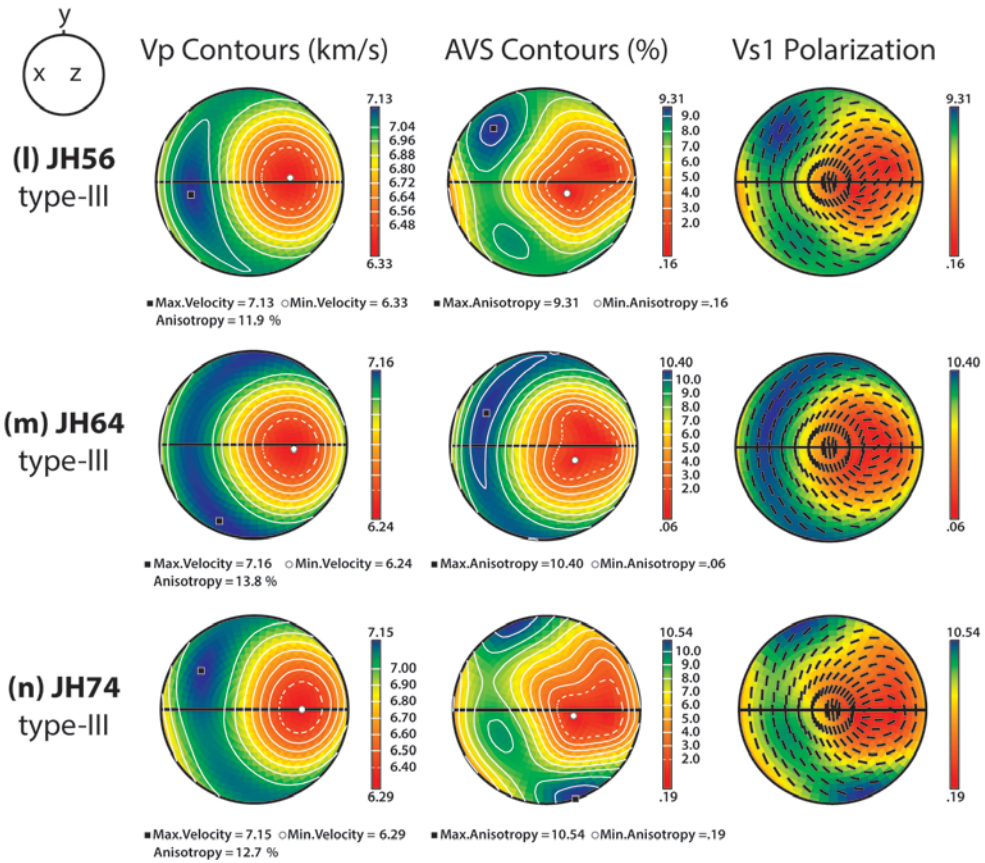


Figure 13. Seismic anisotropy for the flow dipping at 30° to the East from the horizontal flow. Equal area and lower-hemisphere projections were used. The X-direction and the Z-direction are rotated 30° (toward the East) relative to those in Fig. 12. P-wave velocity (Vp), S-wave anisotropy (AVs), and the polarization of the fast shear wave are displayed. Center of pole figure of Vs1 polarization represents the direction of vertically propagating S-wave. Three fabric types show about the same direction of the polarized fast shear wave which is subnormal to the shear direction.

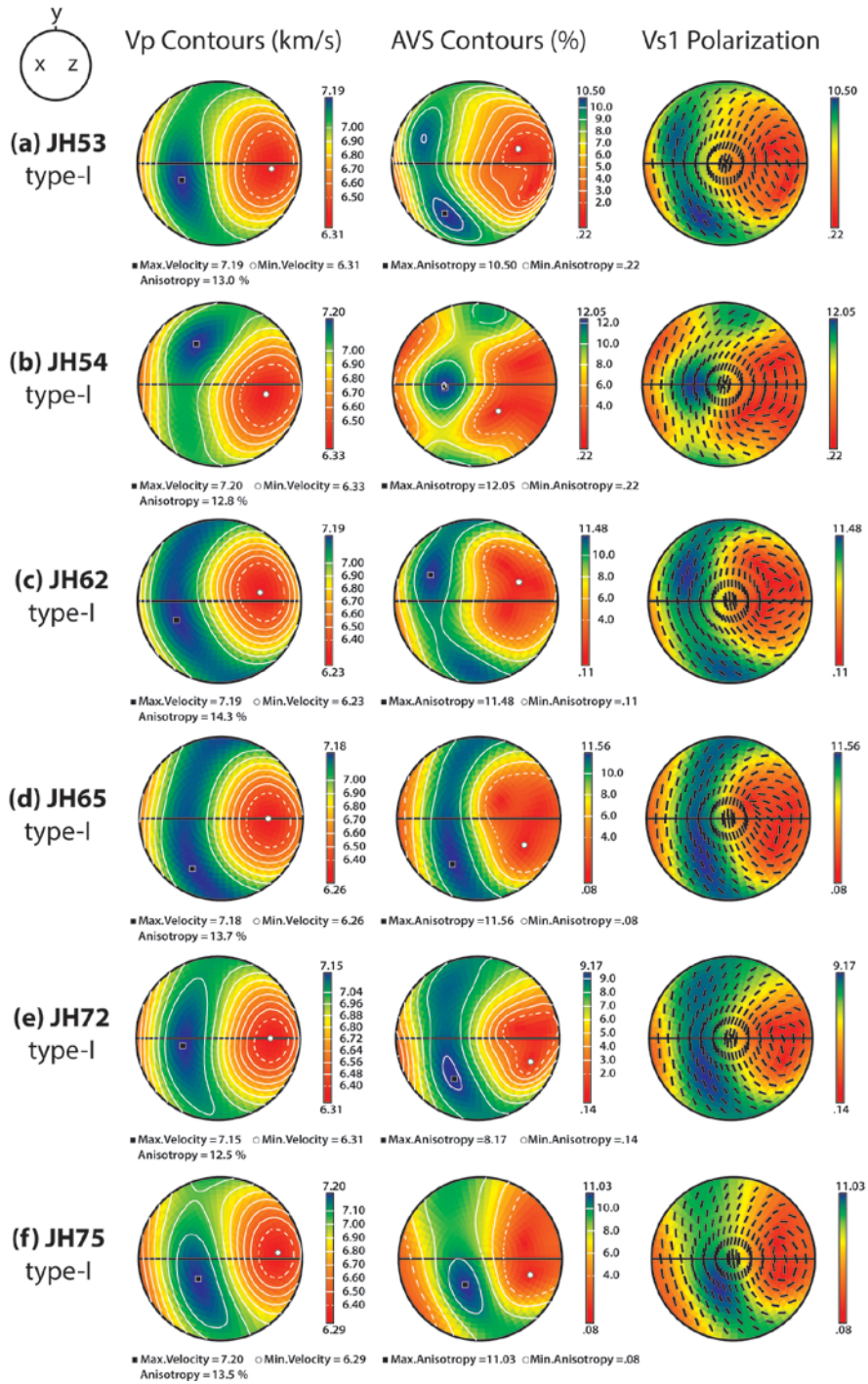


Figure. 14 (Figure caption is in page 43)

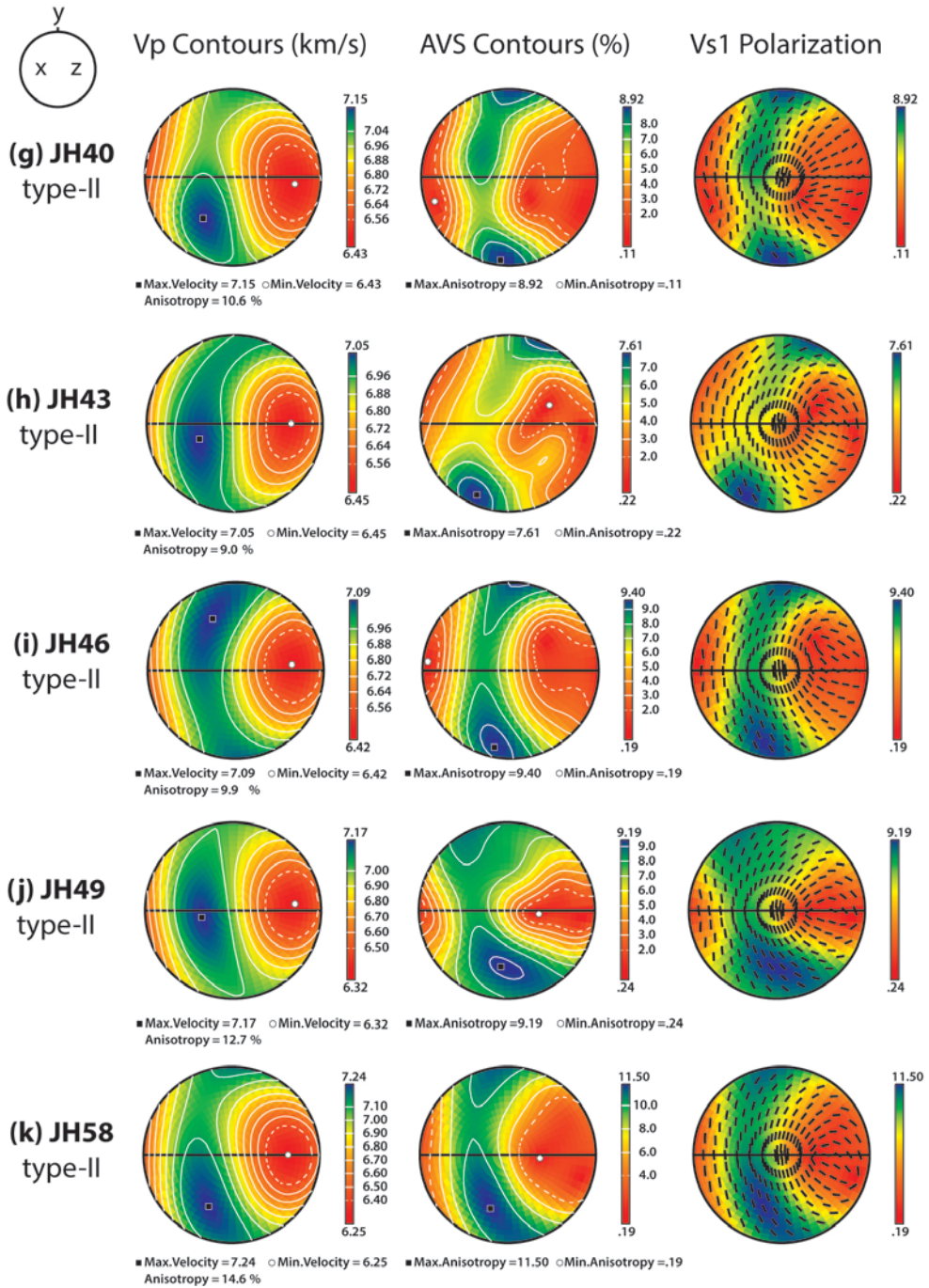


Figure. 14 (Figure caption is in page 43)

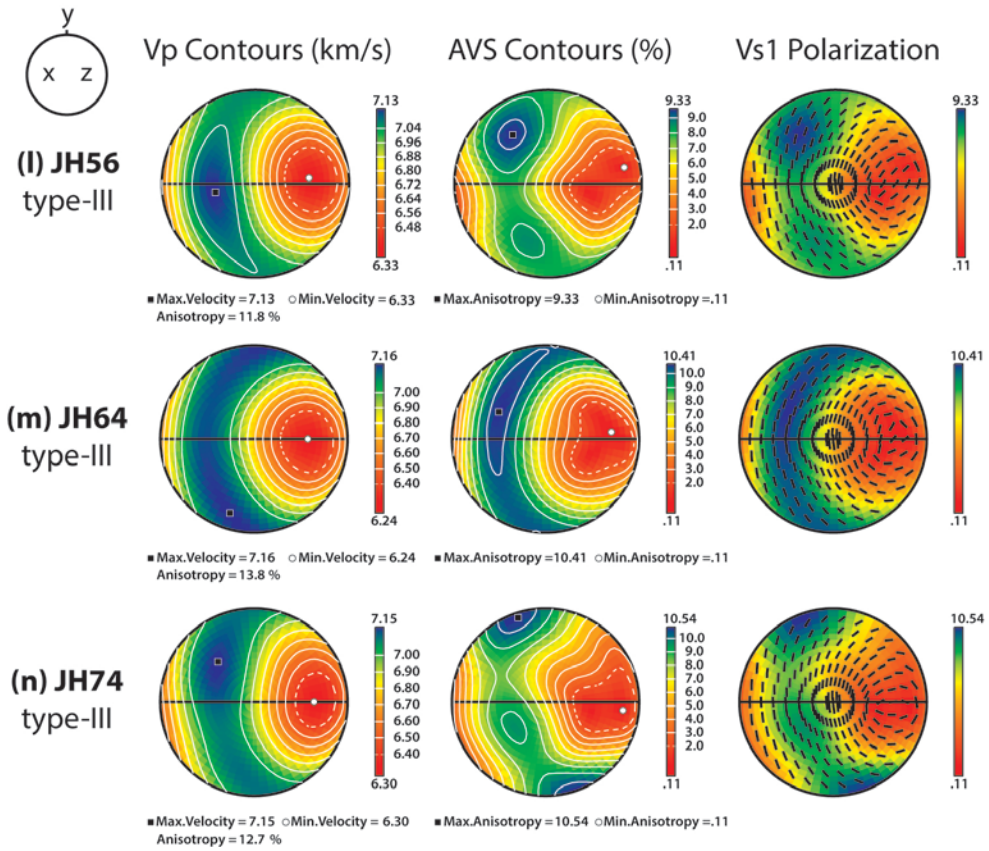


Figure 14. Seismic anisotropy for the flow dipping at 45° to the East from the horizontal flow. Equal area and lower-hemisphere projections were used. The X-direction and the Z-direction are rotated 45° (toward the East) relative to those in Fig. 12. P-wave velocity (V_p), S-wave anisotropy (AVs), and the polarization of the fast shear wave are displayed. Center of pole figure represents the direction of vertically propagating S-wave. Three fabric types show about the same direction of the polarized fast shear wave which is subnormal to the shear direction.

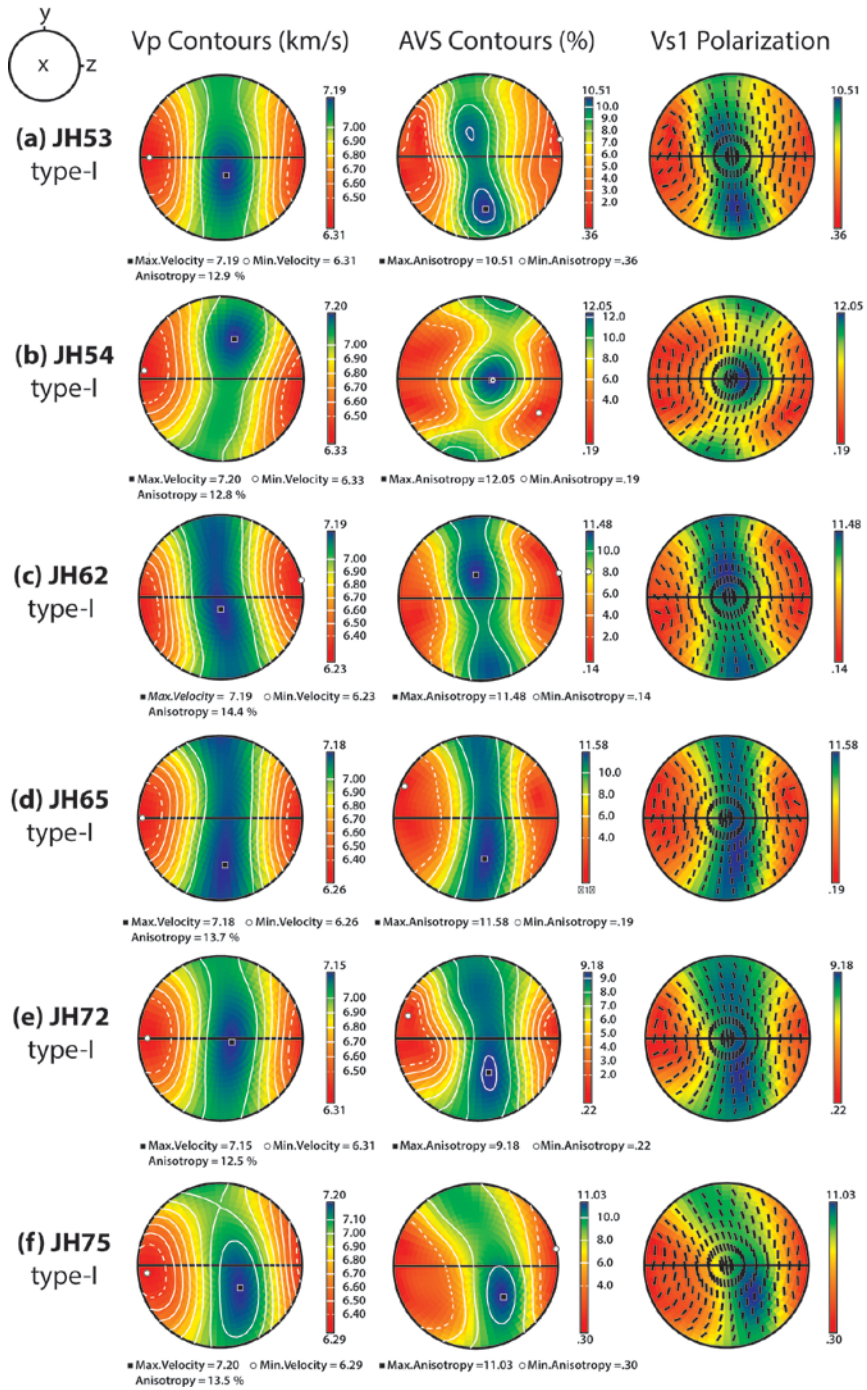


Figure. 15 (Figure caption is in page 46)

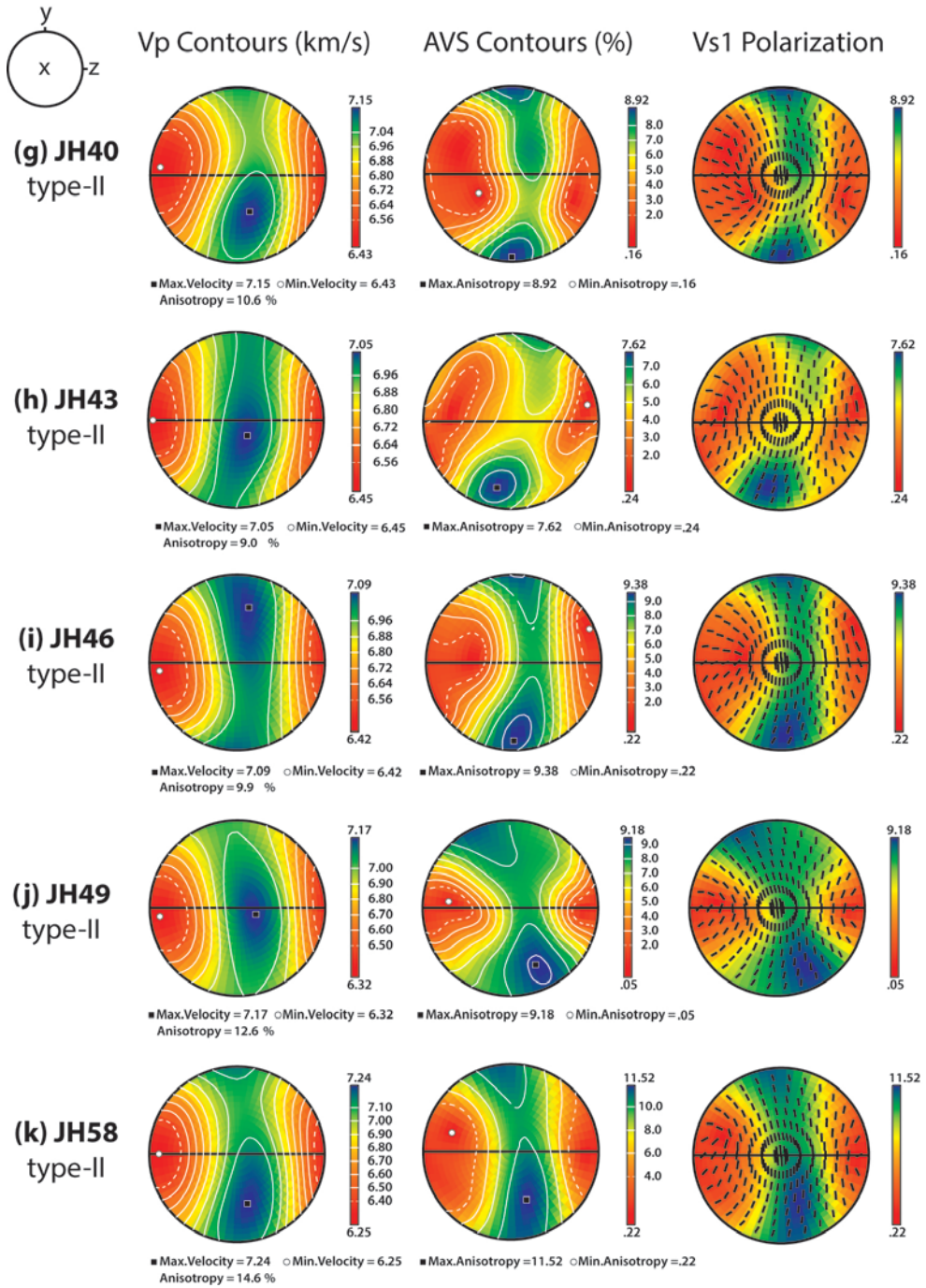


Figure. 15 (Figure caption is in page 46)

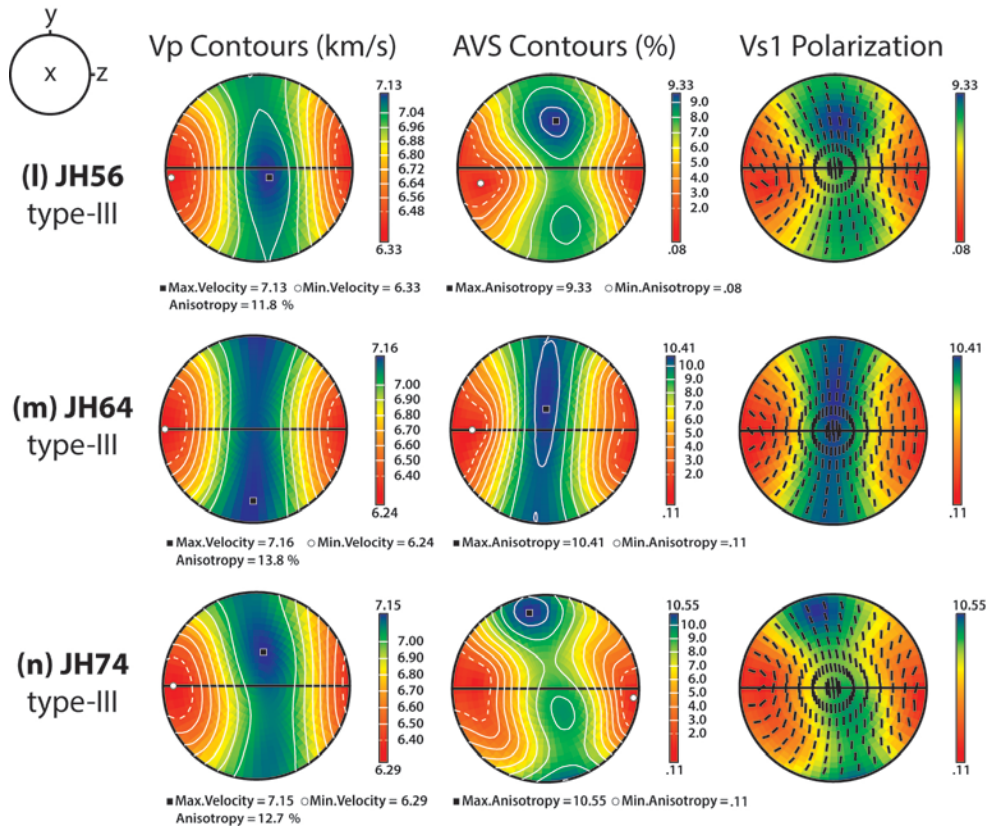


Figure 15. Seismic anisotropy in the vertical flow. Equal area and lower-hemisphere projections were used. The X-direction and the Z-direction are rotated 90° (toward the East) relative to those in Fig. 12. P-wave velocity (Vp), S-wave anisotropy (AVs), and the polarization of the fast shear wave are displayed. Center of pole figure represents the direction of vertically propagating S-wave. Three fabric types show about the same direction of the polarized fast shear wave which is subnormal to the shear direction.

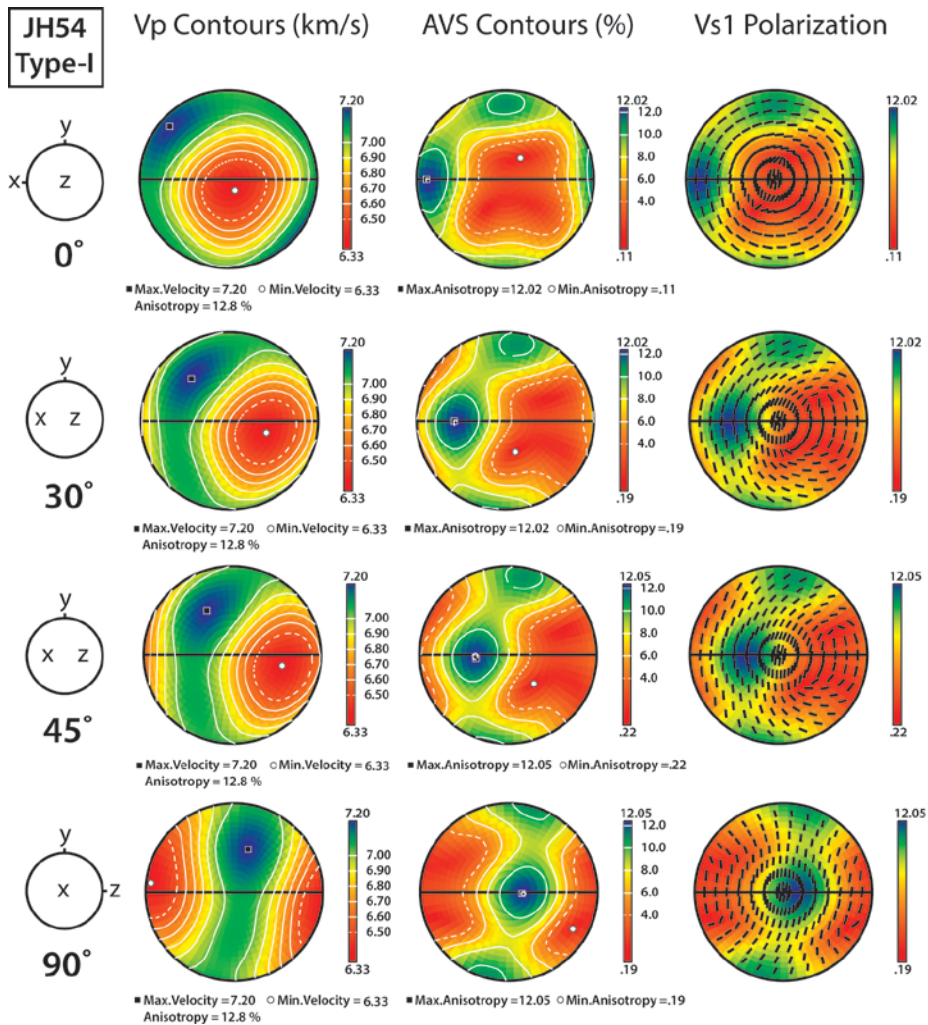


Figure 16. Seismic anisotropy calculated from the CPO of deformed amphibole (JH54; deformed at 1 GPa and 480 °C under dry condition). The X-direction and the Z-direction correspond to the shear direction and the direction normal to the shear plane, respectively. Center of pole figure of Vs1 polarization represents the direction of vertically propagating S-wave. Four different flow geometries are shown dipping at 0 to 90 ° toward the East.

Chapter 6. Discussion

6.1 Deformation mechanism

Brittle processes found in deformed amphibolites can be divided into three stages (Stage1, 2, and 3; Figs. 17 – 19). At Stage1, R' shear is developed at high angles ($40 - 85^\circ$) to the shear plane, forming fractures or narrow shear bands. At Stage2, R shear is developed at low angles ($10 - 20^\circ$) to the shear plane, forming initially narrow shear bands where micro-cracking and grain-size reduction occur. Some shear bands developed into faults. These shear bands themselves eventually become shear zone boundaries which distinguish different domains. Each domain has a different degree of deformation (Fig. 17). This difference is large at the early stage, but becomes smaller as strain proceeds (i.e. highly deformed area becomes broaden, especially during Stage3). Plagioclase appeared to be deformed by brittle or semi-brittle processes. Basically, elongated structures imply that plagioclase was deformed by plastic deformation. But, many fractures across both hornblende and plagioclase indicate that fracturing on plagioclase was resulted from the brittle behavior of hornblende. To identify whether plagioclase experienced only brittle processes without plasticity, observations by transmission electron microscope (TEM) must be followed. On the other hand, hornblende shows

typical features of brittle failure. Hornblende aggregates are fractured by R and R' shear, the fragments of which were deformed by frictional sliding and rotation. Fig. 18 shows two models of frictional sliding of hornblende. Sliding along fracture planes of R' shear is more commonly observed than that of R shear. The rotation of broken grains of hornblende could be achieved in weaker plagioclase matrix. Strain markers and elongated plagioclase aggregates of deformed samples show the progressive rotation of slip plane. At Stage3, C-surface is developed with the localized shear zone nearly parallel to the shear plane, in which, slip plane is suddenly changed to be parallel to the shear plane (Fig. 19). In this stage, grain-size is severely reduced. Broken grains flow cataclastically and rotate on the shear plane.

Brittle behavior of amphibolite in the present study are in good agreement with previous studies on naturally and experimentally deformed amphibole and feldspar (e.g Allison and La Tour, 1977; Nyman et al., 1992; Lafrance and Vernon, 1993; Babaie and La Tour, 1994; Tullis and Yund, 1977, 1987, 1992). Other authors have proposed brittle deformation along with diffusive-mass transfer (Berger and Stunitz, 1996, Imon et al., 2002, 2004, Diaz Aspiroz et al., 2007) and crystal plasticity (Rooney et al.,1970, 1975; Dollinger and Blacic, 1975; Biermann and Van Roermund, 1983; Cumbest et al., 1989; Skrotzki, 1992; Diaz Aspiroz et al., 2007; Cao et al., 2010) as the dominant

deformation mechanism of amphibole.

6.2 The development of CPOs of hornblende

Fig. 20 exhibits three different regions where each fabric type is dominant (see also typical fabric types in Fig. 21). Type-I fabric is dominant at low temperatures (480 to 550 °C), but also found at middle temperatures (590 to 600 °C) with low differential stress (below 60 MPa). Type-II is dominant at middle to high temperatures (590 to 700 °C) with high differential stress (above 110 MPa). Type-III is dominant at high temperatures (640 to 700 °C) with low differential stress (below 130 MPa). On the other hand, it is possible that type-III fabric is a transitional fabric between type-I and type-II fabrics because type-III fabric seems to be somewhat a mixture of type-I and type II fabrics.

Three fabric types of amphibole found in the present study have been observed in naturally deformed amphibole. Type-I is the most commonly found fabric in natural rocks deformed at amphibolite facies conditions (e.g. Mainprice and Nicolas, 1989; Siegesmund et al., 1989; Ji et al., 1993; Berger and Stunitz, 1996; Barruol and Kern, 1996, Kern et al., 2001, Imon et al., 2004; Diaz Aspiroz et al., 2007; Tatham et al., 2008; Cao et al., 2010; Llana-Funez and

Brown, 2012). Most of these studies had shown P-T conditions of the formation of type-I fabric in the ranges of pressures of ~0.5 to 1 GPa and temperatures of ~300 to 700°C.

The other fabric types (type-II and -III) were rarely found in natural rock. Cao et al. (2010) reported type-II fabric for only porphyroclasts deformed by rigid-body rotation. Diaz Aspiroz et al. (2007) observed type-III fabric for one amphibolite sample. Interestingly, Keppler et al., (2013) observed three different hornblende fabrics in retrograde eclogite samples corresponding to type-I, -II, and -III fabrics in this study. However, because of few reports of these fabric types, analyzing formation conditions of each fabric type is inevitably limited.

As Tatham et al. (2008) pointed out, CPO types of amphibole seem to be independent of deformation mechanisms. This is due to the fact that the same CPO types of naturally deformed amphibole found in many studies were thought to be deformed by different mechanisms (e.g. Allison and La Tour, 1977; Diaz Aspiroz et al., 2007; Cao et al., 2010) although some studies suggested that CPO types of amphibole depend on deformation mechanisms (e.g. Diaz Aspiroz et al., 2007; Cao et al., 2010). For example, Diaz Aspiroz et al. (2007) suggested that type-I fabric was formed by diffusive-mass transfer and cataclastic flow, whereas Cao et al. (2010) maintained that crystalline

plasticity formed type-I fabric.

6.3 Water-induced weakening of amphibolite

In spite of the essential hydroxyl group in the amphibole structure, dehydration reaction didn't happen during deformation experiments since the breakdown temperature of hornblende is $\sim 800^{\circ}\text{C}$. Unfortunately, we couldn't measure the water content of amphibolite after the deformation because the deformed sample was not able to be polished thin enough for the transmitted light of a Fourier-transform infrared spectrometer (FTIR) to pass through the sample due to the very fine grain size ($< 5\ \mu\text{m}$) in the sample with the weak bond strength of the grains. However, the prominent strength reduction was observed in the experiments with the added water. When experiments were performed with added water differential stress decreased by approximately 67% compared to those without added water at the same conditions (Fig. 7; Table 2), implying that amphibole strength can be very sensitive to free water during deformation. This water-induced weakening of amphibolite coincides with the earlier experimental results (Riecker and Rooney, 1969; Rooney and Riecker, 1973; Hacker and Christie, 1990).

6.4 Implications for seismic anisotropy

P- and S- wave anisotropies up to $AV_p = 14.6 \%$ and $AV_s = 12.1 \%$ in this study indicate that amphibole can be a major contributor of strong seismic anisotropy at amphibolite facies conditions as previous studies have suggested (e.g. Siegesmund et al., 1989; Tatham et al., 2008; Moschetti et al., 2010).

The result of polarization anisotropy of S-wave shows that the polarization direction and degree of anisotropy of the fast shear wave (V_{s1}) depend on flow geometry rather than amphibole fabric types formed by different conditions. In a horizontal flow, the fast shear wave polarization anisotropy ($1.3 \pm 0.1 \%$ on average; Table 3) for vertically propagating S-wave is too small to accentuate the fact that type-I and type-II fabrics show the opposite directions of the polarized V_{s1} (Fig. 12). However, considering a dipping angle of $\geq 30^\circ$ from the horizontal flow, the same directions of the polarized V_{s1} were obtained from three fabric types, which are subnormal to the shear direction for vertically propagating S-wave. Furthermore, they show much higher anisotropy (e.g. up to 8.5% for the flow dipping angle 45°) than those (up to 2.3%) in the horizontal flow (Table 3). This is because a-axis ([100] axis), the slowest axis of hornblende (Fig. 22), contributes the most to shear wave splitting: tilting at $\geq 30^\circ$ from the horizontal plane, the polarization of the fast shear wave can avoid the effect of a-axis (Figs. 12 - 15), showing the dramatic

change in the polarization direction and the increase in polarization anisotropy.

These results provide important implications for seismic anisotropy. For instance, trench-parallel anisotropy observed in subduction zones (Long and Silver, 2008; Long, 2013) can be attributed to the CPO of deformed amphibole (Fig. 23b). Amphibole in the subducting slab and in the hydrated mantle wedge (25 to 75 km depth; Schmidt and Poli, 1998) may show type-I fabric under low temperature, and amphibole in the mantle wedge at high temperature and high stress condition may show type-II fabric, both of which will produce trench-parallel seismic anisotropy because of the dipping angle of the flow tilted more than 30 ° from the horizontal plane.

Another implication for seismic anisotropy is in the continental crust (Fig. 23a). According to the present study, deformed amphibole in the crust can produce any fabric types found in this study depending on temperature and differential stress. Amphibole CPO in the crust can explain strong P- and S-waves anisotropies up to 14.6 % and 13.0 %, respectively. For horizontal flow, type-I fabric (exception: JH65 for P-wave; JH53 for S-wave) represents that the directions of the maximum P- wave velocity and S-wave anisotropy are subparallel to the shear direction. Type-II fabric shows that the directions of the maximum P-wave velocity and S-wave anisotropy are subparallel and subnormal to the shear direction, respectively. Type-III displays that the

directions of the maximum P- wave velocity and S-wave anisotropy are randomly oriented. However, the directions of the minimum P-wave velocity and S-wave anisotropy of all fabric types, show the same orientation which is nearly perpendicular to the shear plane. In addition, the polarization anisotropy of shear wave can be very different depending on flow geometry. In a horizontal shear, relatively small anisotropy of the polarized fast shear wave up to $AVs = 2.3 \%$ for vertically propagating S-wave (JH40; Table 3), the contribution of which can be limited to account for large delay times observed in the crust. In contrast, in a vertical shear, amphibole can be attributed to the strong shear wave polarization in the crust such that the polarization direction of the fast shear wave becomes subnormal to the shear direction on the shear plane with very high anisotropy up to $AVs = 12.3 \%$ (JH54; Fig. 15; Table 3).

On the other hand, plagioclase, as a secondary phase of amphibolite, seems to play a limited role in seismic anisotropy, whereas it can be involved in the deformation mechanism of amphibole (Berger and Stunitz, 1996; Kruse and Stunitz, 1999; Diaz Aspiroz et al., 2007). Seismic anisotropy of plagioclase was not calculated in the present study because the CPO of plagioclase was not measured. Tatham et al. (2008) showed that the effect of second phase of amphibolite, such as plagioclase, and quartz on seismic anisotropy is merely to attenuate the intensity of anisotropy of the whole rock because of their weak

CPO strength. This supports that seismic anisotropy in the deep crust is mostly dominated by amphibole.

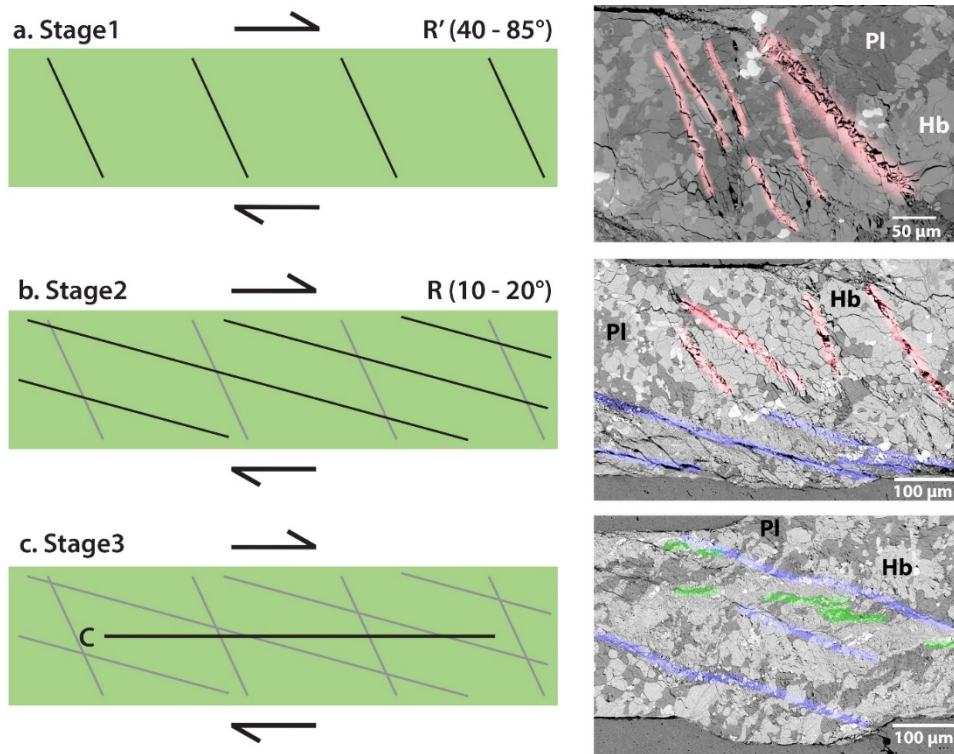


Figure 17. Schematic diagrams showing three stages of deformation (left) and BSE images (right) of deformed amphibolites (JH58 for the top image; JH53 for the middle and the bottom images). Green box corresponds the deformed amphibolite. Sense of shear is indicated by arrows. a) Deformation stage1 is described. The BSE image shows R' shear with fractures (reddishly shaded). b) Deformation stage2 is described. The BSE image shows R shear with shear band and fractures (blue shaded) c) Deformation stage3 is described. The BSE image shows the flow direction of plagioclase parallel the shear plane (greenly shaded). Dark- and light-grey minerals in BSE images indicate plagioclase (Pl) and hornblende (Hb), respectively.

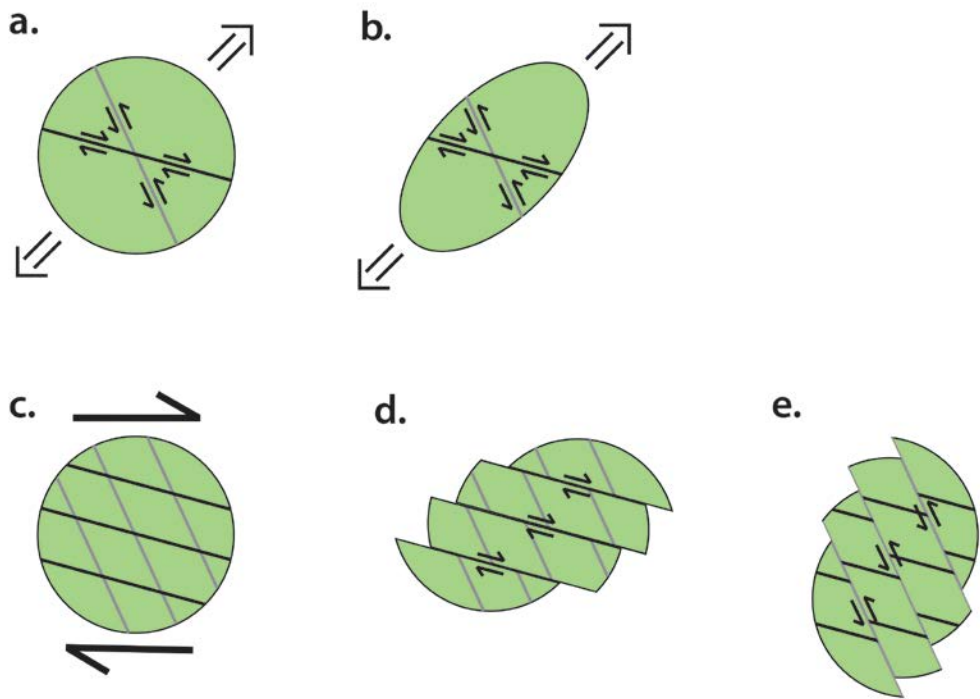


Figure 18. Schematic diagrams of deformation of plagioclase (a, b) and hornblende (c – e) at deformation stage2. a, b) Plagioclase aggregates are elongated by R and R' shear c) Hornblende grains are fractured by R and R' shear during deformation stage2. d, e) Ideal models of frictional sliding of hornblende. d) Sliding along fracture planes of R shear. e) Sliding along fracture planes of R' shear.

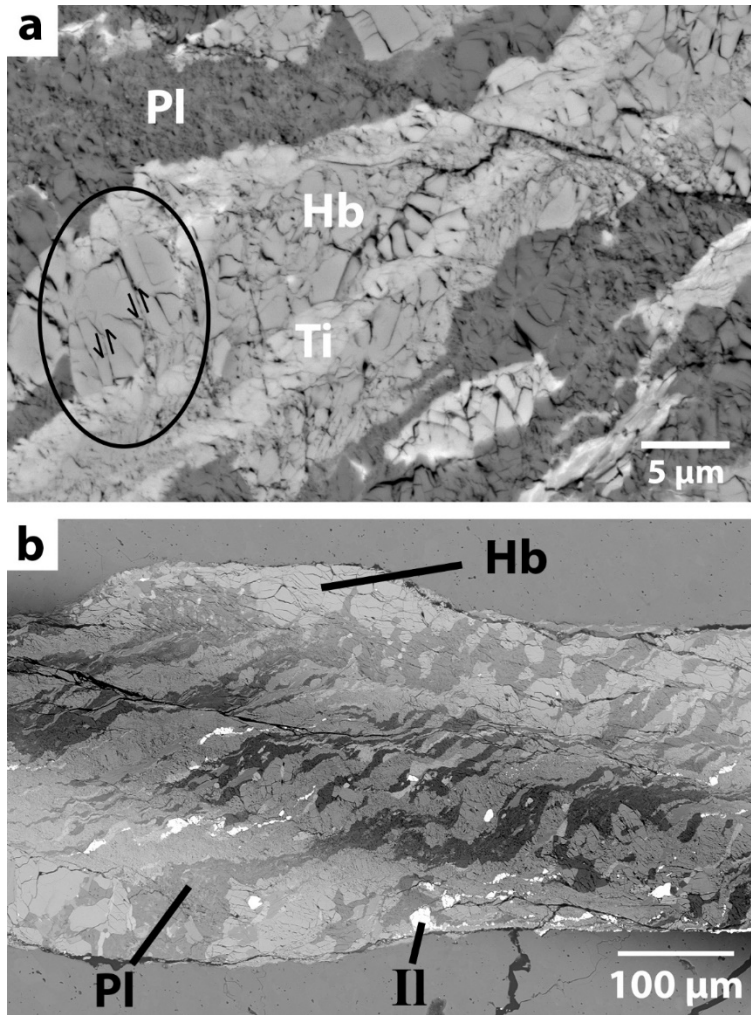


Figure 19. BSE images of the deformed amphibolite (a: JH58; b: JH54). a) The black ellipse indicates frictional sliding along fracture planes of R' shear. b) The dark area (diagonally shaded across the sample) shows the band shaped flow of plagioclase aggregates indicating a sharp change of slip plane between deformation stage2 and stage3. Hb: hornblende; Pl: plagioclase; Ti: titanite; Il: ilmenite.

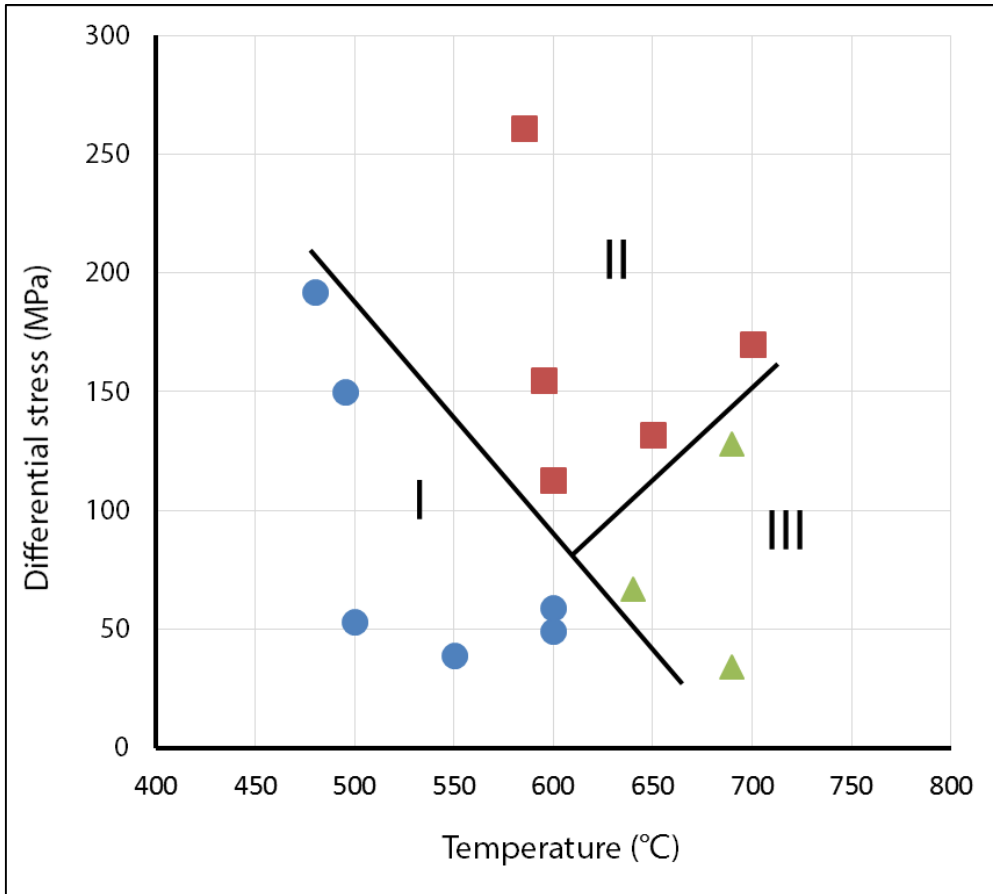


Figure 20. A fabric diagram for the deformed amphibole. X-axis represents temperatures during deformation experiments. Y-axis represents the peak value of differential stress after yielding. The circle, square, and triangle indicate type-I, type-II, and type-III fabrics, respectively.

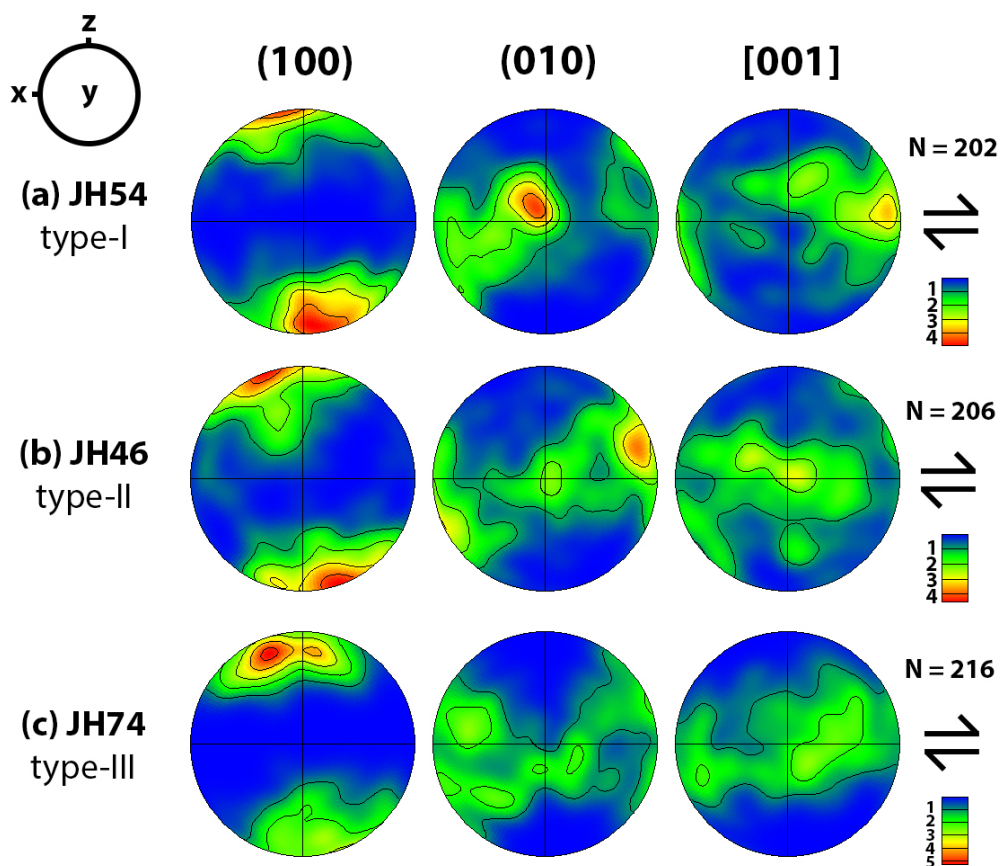


Figure 21. Pole figures of crystallographic preferred orientation (CPO) of deformed amphibole. Three typical CPO types are displayed. Pressure during deformation was 1 GPa. (a) Type-I. (b) Type-II. (c) Type-III. The X-direction and the Z-direction correspond to the shear direction and the shear plane normal, respectively. The arrows indicate the dextral shear sense. The pole figures are equal-area upper-hemisphere projections with a half-width of 20° . “N” indicates data points measured in each sample.

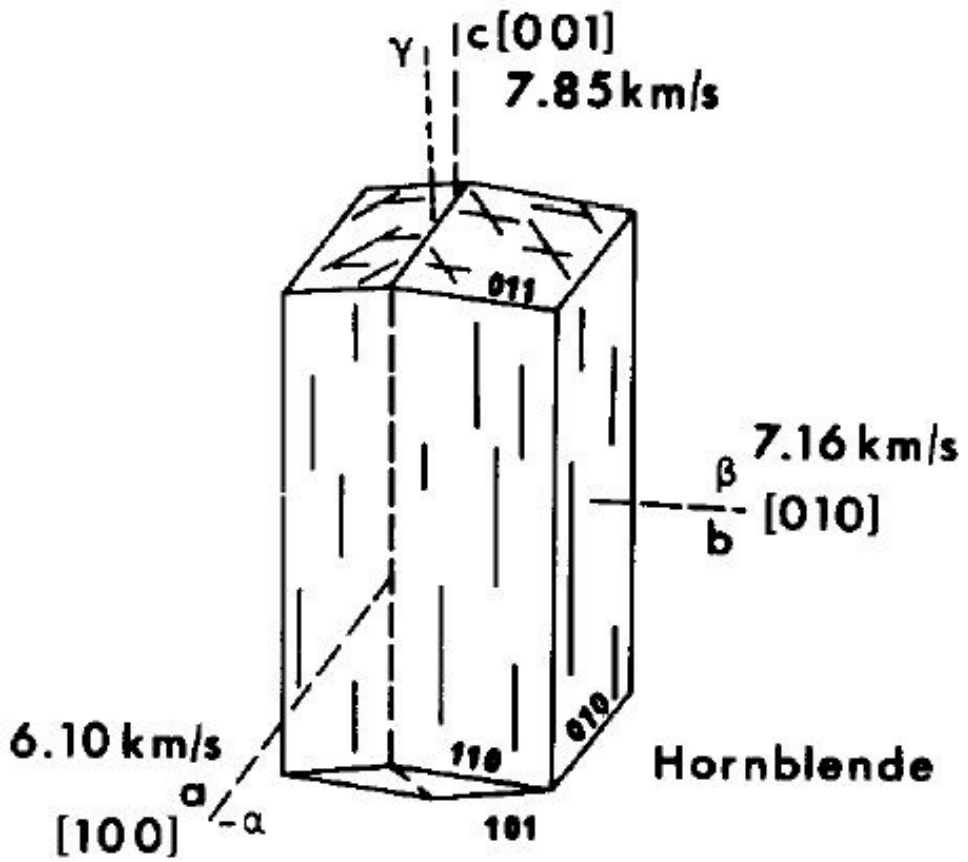


Figure 22. A Schematic diagram of relationship between optical (α , β , and γ) and crystallographic (a , b , and c) axes and calculated velocities (Siegesmund et al., 1989).

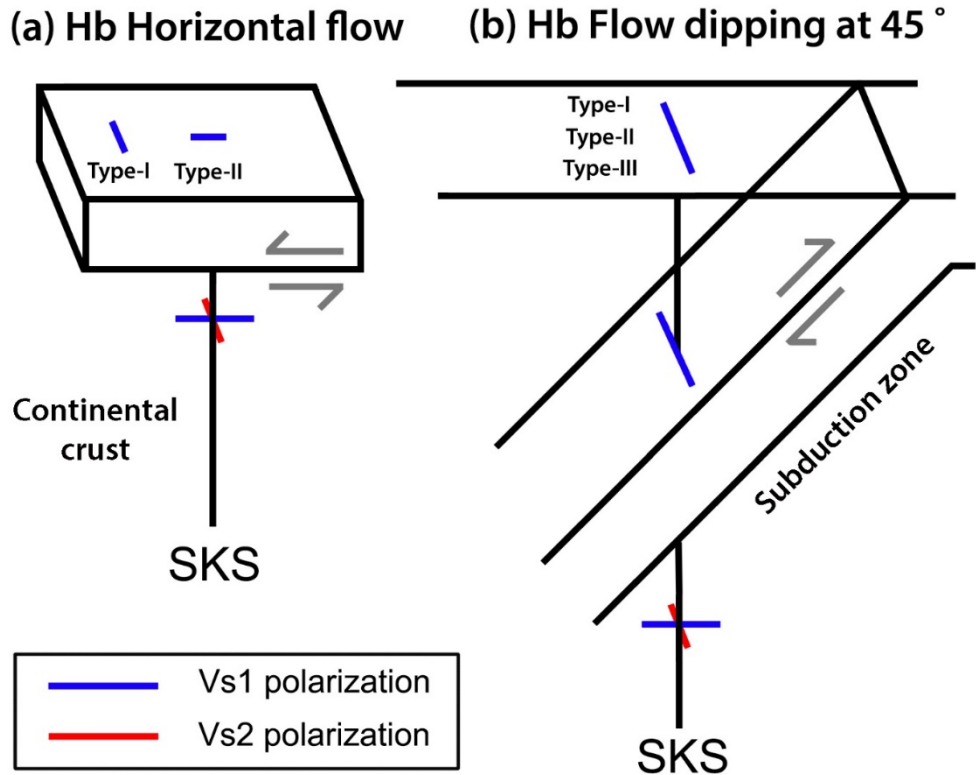


Figure 23. A schematic diagram showing the polarization direction of shear wave for vertically propagating S-wave (SKS). Hb: hornblende (a) In horizontal flow, the polarization direction of the fast shear wave (Vs1) is normal and parallel to the flow direction for the type-I and -II CPOs of amphibole, respectively, with lower anisotropy. (b) For the flow dipping at 45°, the polarization direction of the fast shear wave (Vs1) is parallel to trench and normal to the flow direction for all three types of CPOs of amphibole with higher anisotropy. Blue bar represents the polarization direction of fast shear wave (Vs1). Red bar indicates polarization direction of slow shear wave (Vs2).

7. Conclusion

The simple-shear deformation experiments of natural amphibolite were carried out at the pressure of 1 GPa and temperatures of 480 to 700 °C. The dominant deformation mechanism of amphibole appeared cataclastic flow accompanied by mechanical rotation of fractured grains, the size of which became very fine (less than 5 μm). Plagioclase, the second phase of the deformed amphibolite was plastically deformed with fracturing, but no sign of crystal plasticity for amphibole was observed.

Three types of crystallographic preferred orientation (CPO) of hornblende were obtained depending on temperature and differential stress. At relatively low temperature (480 to 550 °C), type-I fabric was dominant. At higher temperature (600 to 700 °C), type-II fabric was dominant in high stress regime (113 to 261 MPa), while type-III fabric was dominant in low stress regime (34 to 128 MPa).

Seismic anisotropy calculated from the CPOs of deformed hornblende revealed that amphibole can produce significant seismic anisotropy in the lower crust and upper mantle. In addition, the direction and degree of the fast shear wave anisotropy can be different depending on flow geometry. In a horizontal flow, the polarization direction changes among different fabric

types, and the polarization anisotropies for all fabric types are somewhat limited up to 2.3 %. For the flow dipping at $\geq 30^\circ$ from the horizontal plane, the polarization direction of the fast shear wave displays about the same direction regardless of fabric types, which is subnormal to the shear direction, with high anisotropies up to 12.3 % (for a vertical flow); the shear wave anisotropy increases with the increasing dipping angle of flow.

References

- Aleksandrov, K. S. and T. V. Ryzhova (1961). "The elastic properties of rock-forming minerals, 1: pyroxenes and amphiboles." *Bulletin of Academy of Sciences USSR, Geophysical Series* **871-875**: 1339-1344.
- Allison, I. and T. E. L. Tour (1977). "Brittle deformation of hornblende in a mylonite: a direct geometrical analogue of ductile deformation by translation gliding." *Canadian Journal of Earth Sciences* **14**(8): 1953-1958.
- Babaie, H. A. and T. E. La Tour (1994). "Semibrittle and cataclastic deformation of hornblende-quartz rocks in a ductile shear zone." *Tectonophysics* **229**(1): 19-30.
- Banda, E., et al. (1981). "Crust and upper mantle structure of the central Iberian Meseta (Spain)." *Geophysical Journal of the Royal Astronomical Society* **67**(3): 779-789.
- Barruol, G. and H. Kern (1996). "Seismic anisotropy and shear-wave splitting in lower-crustal and upper-mantle rocks from the Ivrea Zone—experimental and calculated data." *Physics of the earth and planetary interiors* **95**(3): 175-194.
- Barruol, G. and D. Mainprice (1993). "3-D seismic velocities calculated

- from lattice-preferred orientation and reflectivity of a lower crustal section: examples of the Val Sesia section (Ivrea zone, northern Italy)." *Geophysical Journal International* **115**(3): 1169-1188.
- Berger, A. and H. Stünitz (1996). "Deformation mechanisms and reaction of hornblende: examples from the Bergell tonalite (Central Alps)." *Tectonophysics* **257**(2): 149-174.
- Biermann, C. and H. Van Roermund (1983). "Defect structures in naturally deformed clinoamphiboles—a TEM study." *Tectonophysics* **95**(3): 267-278.
- Boland, A. and R. Ellis (1991). "A geophysical model for the Kapuskasing uplift from seismic and gravity studies." *Canadian Journal of Earth Sciences* **28**(3): 342-354.
- Braile, L., et al. (1982). "The Yellowstone-Snake River Plain Seismic Profiling Experiment: Crustal structure of the Eastern Snake River Plain." *Journal of Geophysical Research: Solid Earth* (1978–2012) **87**(B4): 2597-2609.
- Cao, S., et al. (2010). "Orientation-related deformation mechanisms of naturally deformed amphibole in amphibolite mylonites from the Diancang Shan, SW Yunnan, China." *Journal of Structural Geology* **32**(5): 606-622.
- Cumbest, R., et al. (1989). "Dynamic recrystallization and chemical

- evolution of clinoamphibole from Senja, Norway." *Contributions to Mineralogy and Petrology* **101**(3): 339-349.
- Díaz Aspiroz, M., et al. (2007). "Development of lattice preferred orientation in clinoamphiboles deformed under low-pressure metamorphic conditions. A SEM/EBSD study of metabasites from the Aracena metamorphic belt (SW Spain)." *Journal of Structural Geology* **29**(4): 629-645.
- Dollinger, G. and J. D. Blacic (1975). "Deformation mechanisms in experimentally and naturally deformed amphiboles." *Earth and Planetary Science Letters* **26**(3): 409-416.
- Goodwin, E. B. and J. McCarthy (1990). "Composition of the lower crust in west central Arizona from three-component seismic data." *Journal of Geophysical Research: Solid Earth* (1978–2012) **95**(B12): 20097-20109.
- Grad, M. and U. Luosto (1987). Seismic models of the crust of the Baltic shield along the SVEKA profile in Finland. *Annales geophysicae. Series B. Terrestrial and planetary physics.*
- Hacker, B. R. and J. M. Christie (1990). "Brittle/ductile and plastic/cataclastic transitions in experimentally deformed and metamorphosed amphibolite." *The Brittle-Ductile Transition in Rocks, Geophys. Monogr. Ser* **56**: 127-147.

- Imon, R., et al. (2004). "Development of shape- and lattice-preferred orientations of amphibole grains during initial cataclastic deformation and subsequent deformation by dissolution–precipitation creep in amphibolites from the Ryoke metamorphic belt, SW Japan." *Journal of Structural Geology* **26**(5): 793-805.
- Iwasaki, T., et al. (1994). "Precise P and S wave velocity structures in the Kitakami massif, Northern Honshu, Japan, from a seismic refraction experiment." *Journal of Geophysical Research: Solid Earth* (1978–2012) **99**(B11): 22187-22204.
- Ji, S., et al. (1993). "Petrofabric, P-wave anisotropy and seismic reflectivity of high-grade tectonites." *Tectonophysics* **222**(2): 195-226.
- Keppler, R., et al. (2013). "Crystallographic preferred orientation and elastic anisotropy of high-pressure rocks from the Eclogite Zone of the Tauern Window, Austria." *American Geophysics Union Abstracts*.
- Kern, H., et al. (2001). "Pressure and temperature dependence of V_P and V_S in rocks from the superdeep well and from surface analogues at Kola and the nature of velocity anisotropy." *Tectonophysics* **338**(2): 113-134.
- Kitamura, K. (2006). "Constraint of lattice-preferred orientation (LPO) on V_p anisotropy of amphibole-rich rocks." *Geophysical Journal International* **165**(3): 1058-1065.

- Kruse, R. and H. Stünitz (1999). "Deformation mechanisms and phase distribution in mafic high-temperature mylonites from the Jotun Nappe, southern Norway." *Tectonophysics* **303**(1): 223-249.
- Lafrance, B., et al. (1993). "Mass transfer and microfracturing in gabbroic mylonites of the Guadalupe igneous complex, California." in; J.N. Boland, J.D. Fitz Gerald (Eds.), *Defects and Processes in the Solid State, Geoscience Applications, the McLaren Volume, Developments in Petrology* **4**: 151-167.
- Leake, B. E. (1978). "Nomenclature of amphiboles." *The Canadian Mineralogist* **16**(4): 501-520.
- Leaver, D. S., et al. (1984). "A seismic refraction study of the Oregon Cascades." *Journal of Geophysical Research: Solid Earth* (1978–2012) **89**(B5): 3121-3134.
- Llana-Funez, S. and D. Brown (2012). "Contribution of crystallographic preferred orientation to seismic anisotropy across a surface analog of the continental Moho at Cabo Ortegal, Spain." *Geological Society of America Bulletin* **124**(9-10): 1495-1513.
- Lloyd, G. E., et al. (2009). "Mica, deformation fabrics and the seismic properties of the continental crust." *Earth and Planetary Science Letters* **288**(1-2): 320-328.
- Long, M. D. (2013). "Constraints on subduction geodynamics from seismic

- anisotropy." *Reviews of Geophysics* **51**(1): 76-112.
- Long, M. D. and P. G. Silver (2008). "The subduction zone flow field from seismic anisotropy: A global view." *Science* **319**(5861): 315-318.
- Luetgert, J. H., et al. (1987). "Wide-angle deep crustal reflections in the northern Appalachians." *Geophysical Journal of the Royal Astronomical Society* **89**(1): 183-188.
- Luosto, U., et al. (1990). "Crust and upper mantle structure along the DSS Baltic profile in SE Finland." *Geophysical Journal International* **101**(1): 89-110.
- Mahan, K. (2006). "Retrograde mica in deep crustal granulites: Implications for crustal seismic anisotropy." *Geophysical Research Letters* **33**(24).
- Mainprice, D. (1990). "A FORTRAN program to calculate seismic anisotropy from the lattice preferred orientation of minerals." *Computers & Geosciences* **16**(3): 385-393.
- Mainprice, D. and A. Nicolas (1989). "Development of shape and lattice preferred orientations: application to the seismic anisotropy of the lower crust." *Journal of Structural Geology* **11**(1): 175-189.
- Meissner, R., et al. (2006). "Seismic lamination and anisotropy of the Lower Continental Crust." *Tectonophysics* **416**(1-4): 81-99.
- Moschetti, M. P., et al. (2010). "Seismic evidence for widespread western-US deep-crustal deformation caused by extension." *Nature*

464(7290): 885-889.

Nyman, M. W., et al. (1992). "Cataclastic deformation mechanism for the development of core-mantle structures in amphibole." *Geology* **20**(5): 455.

Ozacar, A. A. (2004). "Crustal seismic anisotropy in central Tibet: Implications for deformational style and flow in the crust." *Geophysical Research Letters* **31**(23).

Rasolofosaon, P. N. J., et al. (2000). "Characterization of crack distribution: fabric analysis versus ultrasonic inversion." *Geophysical Journal International* **141**(2): 413-424.

Riecker, R. E. and T. P. Rooney (1969). "Water-induced weakening of hornblende and amphibolite." *Nature* **224**: 1299.

Rooney, T. P., et al. (1974). "Mechanical Twinning in Experimentally and Naturally Deformed Hornblende." No. AFCRL-TR-74-0361. AIR FORCE CAMBRIDGE RESEARCH LABS LG HANSCOM FIELD MASS.

Rooney, T. P. and R. E. Riecker (1973). "Constant Strain-Rate Deformation of Amphibole Minerals." No. AFCRL-TR-73-0045. AIR FORCE CAMBRIDGE RESEARCH LABS LG HANSCOM FIELD MASS.

Rooney, T. P., et al. (1975). "Hornblende deformation features." *Geology* **3**(7): 364-366.

- Rooney, T. P., et al. (1970). "Deformation twins in amphibole." *Science* **169**(3941): 173-175.
- Rudnick, R. L. and D. M. Fountain (1995). "Nature and composition of the continental crust: a lower crustal perspective." *Reviews of Geophysics* **33**(3): 267-309.
- Schmidt, M. W. and S. Poli (1998). "Experimentally based water budgets for dehydrating slabs and consequences for arc magma generation." *Earth and Planetary Science Letters* **163**(1): 361-379.
- Shapiro, N. M., et al. (2004). "Thinning and flow of Tibetan crust constrained by seismic anisotropy." *Science* **305**(5681): 233-236.
- Siegesmund, S., et al. (1989). "Anisotropy of Vp and Vs in an amphibolite of the deeper crust and its relationship to the mineralogical, microstructural and textural characteristics of the rock." *Tectonophysics* **157**(1): 25-38.
- Skrotzki, W. (1992). "Defect structure and deformation mechanisms in naturally deformed hornblende." *Physica Status Solidi (a)* **131**(2): 605-624.
- Tatham, D. J., et al. (2008). "Amphibole and lower crustal seismic properties." *Earth and Planetary Science Letters* **267**(1-2): 118-128.
- Tullis, J. and R. Yund (1992). "The brittle-ductile transition in feldspar aggregates: An experimental study." *International Geophysics* **51**: 89-

117.

Tullis, J. and R. A. Yund (1977). "Experimental deformation of dry Westerly granite." *Journal of Geophysical Research* **82**(36): 5705-5718.

Tullis, J. and R. A. Yund (1987). "Transition from cataclastic flow to dislocation creep of feldspar: Mechanisms and microstructures." *Geology* **15**(7): 606-609.

Valdes, C. M., et al. (1986). "Crustal structure of Oaxaca, Mexico, from seismic refraction measurements." *Bulletin of the Seismological Society of America* **76**(2): 547-563.

Weiss, T., et al. (1999). "Seismic velocities and anisotropy of the lower continental crust: A review." *Seismic Exploration of the Deep Continental Crust*: 97-122.

Zelt, B., et al. (1993). "Crustal velocity structure in the eastern Insular and southernmost Coast belts, Canadian Cordillera." *Canadian Journal of Earth Sciences* **30**(5): 1014-1027.

국문요약

자연에서 수집한 각섬암 (amphibolite)으로 1 GPa의 압력과 480 – 700 °C 의 온도에서 modified Griggs apparatus를 사용, 단순 전단 변형 실험 (deformation experiments in simple shear)을 수행하였다. 실험에 사용된 각섬암은 대한민국 경기도 연천의 것으로 약 20 μm 의 작은 입자크기를 가지고 있으며, 주로 각섬석 (hornblende; 68 %)과 회장석 (anorthite; 23 %)으로 이루어져 있다. 실험으로 변형된 각섬암은 반취성 (semi-brittle)의 변형거동 (deformation behavior)을 보였는데, 각섬석의 주 변형 메카니즘은 부서진 입자들의 회전을 동반한 파쇄유동 (cataclastic flow)으로써, 5 μm 이하의 아주 작은 입자크기를 보여 주었다. 변형된 각섬석은 온도와 차동응력 (defferential stress)에 따라 세 가지 유형의 격자선호 방향 (CPO)을 생성하였다. 상대적으로 낮은 온도 (480 - 550 °C)에서는 type-I 만 이 생성되는 반면에, 중간 온도 (590 – 600 °C)에서는 차동응력에 따라 type-I (50 – 60 MPa)과 type-II (110 – 260 MPa)이 생성되었다. 높은 온도 (640 – 700 °C)에서는 type-II와 type-III가 각각 높은 차동응력 (130 – 170 MPa)과 낮은 차동응력 (34 - 128 MPa)의 조건에서 발견되었다. 이렇게 얻어진 격자선호방향들로부터 계

산된 지진파 비등방성 (seismic anisotropy)은 하부지각과 상부맨틀의 각섬석이 강한 지진파 비등방성을 만들 수 있음을 보여 주었다. 또한, 표면에 수직하게 전파하는 빠른 전단파의 편광 방향과 정도는 flow geometry에 따라 달라질 수 있었다. 수평적 flow에서 전단파의 편광방향 (polarization direction)은 격자선호방향의 유형에 따라 바뀌는데, 이 전단파 비등방성의 크기는 최대 2.3 % 로 제한적인 값을 보였다. 그러나 수평적 flow로부터 30 ° 이상의 경사각 (dipping angle)에서는 빠른 전단파의 편광방향이 각섬석의 격자선호방향의 유형과는 상관없이 거의 같은 방향 (전단방향에 거의 수직한 방향)을 보여 주었다. 전단파 비등방성의 크기는 flow의 경사 각도 (0 - 90 °)가 증가할 수록 최대 12.3 %까지 커졌다.

주요어: 각섬석, 단순 전단 변형 실험, 격자선호방향, 지진파 비등방성, 각섬암, modified Griggs apparatus.

학번: 2011-20358